BIOPHYSICS

A gating lever and molecular logic gate that couple voltage and calcium sensor activation to opening in BK potassium channels

Liang Sun and Frank T. Horrigan*

BK channels uniquely integrate voltage and calcium signaling in diverse cell types through allosteric activation of their K^+-conducting pore by structurally distinct V and Ca^{2+} sensor domains. Here, we define mechanisms and interaction pathways that link V sensors to the pore by analyzing effects on allosteric coupling of point mutations in the context of Slo1 BK channel structure. A gating lever, mediated by S4/S5 segment interaction within the transmembrane domain, rotates to engage and stabilize the open conformation of the S6 inner pore helix upon V sensor activation. In addition, an indirect pathway, mediated by the carboxyl-terminal cytosolic domain (CTD) and C-linker that connects the CTD to S6, stabilizes the closed conformation when V sensors are at rest. Unexpectedly, this mechanism, which bypasses the covalent connections of C-linker to CTD and pore, also transduces Ca^{2+}-dependent coupling in a manner that is completely nonadditive with voltage, analogous to the function of a digital logic (OR) gate.

INTRODUCTION

Large-conductance V- and Ca^{2+}-activated BK potassium channels (also known as KCa1.1, MaxiK) are widely expressed and important for regulating processes that integrate V and Ca^{2+} signaling, such as neuronal excitability (*1*, *2*), hormone release (*3*, *4*), and smooth muscle tone (*5*, *6*). Similar to purely V-dependent K^+ (K_V) channels, BK channels are composed of four identical α subunits (Slo1), with an S1-S4 voltage sensor domain (VSD) and S5-S6 pore-gate domain (PGD). However, BK channels also have an additional S0 transmembrane segment and large C-terminal cytosolic domain (CTD). The CTD is directly connected to the pore-lining S6 segment by a C-linker, is composed of two homologous RCK domains in each subunit (RCK1 and RCK2; Fig. 1A and fig. S1, A and B), and assembles to form a tetrameric gating ring structure that expands upon Ca^{2+} binding (*7*, *8*). Together with these structural differences, BK channels exhibit distinct functional properties compared to K_V channels, including not only sensitivity to intracellular Ca^{2+} but also reduced V dependence and fundamental differences in the mechanisms that couple VSD activation to PGD opening (i.e., electromechanical coupling). Although most charged residues in the VSD of K_V channels are conserved in Slo1, both the number of residues that contribute to gating charge and the magnitude of their individual contributions are less, suggesting that the VSD of BK channels undergoes different and more limited conformational changes than that of K_V channels (*9*). In addition, while K_V channel gating is well described in terms of obligatory coupling mechanisms that require all V sensors to activate before channels can open (*10*), BK channels can open at low probability in the absence of V sensor activation, a phenomenon best described by allosteric models of electromechanical coupling, such as the Horrigan-Aldrich (HA) model (*11*, *12*), which assume that VSD and PGD can undergo nonobligatory conformational changes that are energetically coupled.

Department of Integrative Physiology, Baylor College of Medicine, Houston, TX 77030, USA.
*Corresponding author. Email: horrigan@bcm.edu

In line with functional differences in electromechanical coupling, BK and K_V channels exhibit structural differences in the interaction between VSD and PGD. Most K_V channels (K_V1 to K_V9) exhibit a domain-swapped architecture, with VSD/PGD contacts occurring between neighboring subunits, including canonical interactions mediated by the S4-S5 linker and S6 segment that are thought to be critical for electromechanical coupling (*13*, *14*). By contrast, BK channels exhibit a non–domain-swapped VSD/PGD arrangement and a different S4-S5 linker structure (*15*). In K_V channels, the S4-S5 linker adopts a long α-helical structure that forms a cuff around the pore and is hypothesized to transmit force from the VSD to the pore to control opening and closing directly. In Slo1, the S4-S5 linker is a short ordered loop (*15*), raising questions whether it plays the same role (*16*). Conversely, some VSD/PGD contacts in Slo1, especially between S4 and S5, are more extensive than in K_V channels, suggesting that noncanonical pathways for direct VSD/PGD interaction could exist in BK channels. Last, the CTD of Slo1 may play a unique role in electromechanical coupling as it makes extensive contact with both VSD and PGD and can potentially mediate indirect interaction between transmembrane domains (TMDs). Consistent with this hypothesis, truncation of Slo1 to remove the CTD, or a mutation (L390P) at the CTD/VSD interface, reduces electromechanical coupling (*17*, *18*), whereas Mg^{2+} enhances coupling (*19*) by binding at the CTD/VSD interface (*20*).

What is the molecular basis for the differences in electromechanical coupling between BK and K_V channels? Does the S4-S5 linker of BK channels play the same role as in K_V channels and, if not, how is energy transferred from VSDs to PGD within the TMD? If the CTD also plays a role in electromechanical coupling, and the CTD expands upon Ca^{2+} binding (altering the VSD/CTD interface), then how is it possible that voltage and Ca^{2+} appear to have virtually independent and additive effects on BK channel activity (*12*, *21*, *22*)? To address these and other questions, we performed an alanine scan of mSlo1, guided by hSlo1 structure, including the S4-S5 linker region, S6 tail, C-linker, and part of the RCK1 domain, to determine the contribution of these regions to V- and

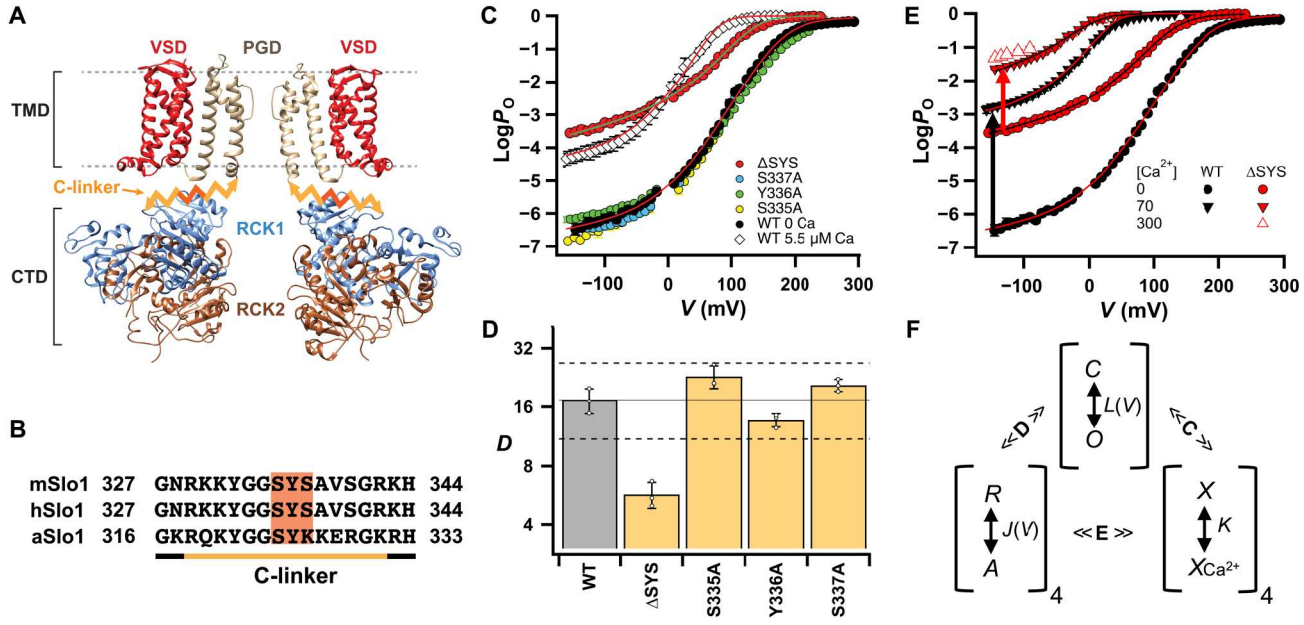

Fig. 1. Shortening the C-linker increases P_O while reducing electromechanical coupling. (**A**) Apo structure of human BK channel, hSlo1 (6V3G), highlighting different domains. For clarity, domains in the front and back have been removed such that adjacent TMD and CTD domains are from different subunits. For illustration purposes, the C-linker is depicted as a spring connecting the adjacent S6 tail and RCK1, but in reality, this connection occurs within the same subunit (fig. S1). (**B**) C-linker sequence alignment for mouse, human, and aplysia Slo1 orthologs highlighting location of SYS deletion. (**C**) Log(P_O)-V relations (mean ± SEM) in 0 Ca^{2+} for ΔSYS, S335A, Y336A, S337A, and WT in 0 and 5.5 μM Ca^{2+}. Solid curves represent HA model fits for WT and ΔSYS. (**D**) Allosteric coupling factor D (mean ± SD) estimated from HA model fits and $q_{\lambda MAX}$ method as described in the text (open circles are individual estimates) is plotted on a log scale to reflect coupling energy, with dashed lines representing 3 SDs from the WT mean. (**E**) Mean log(P_O)-V relations and fits for ΔSYS, and WT in different Ca^{2+}, with arrows representing the Ca^{2+}-dependent increase in log(P_O) at −120 mV, illustrating the reduced Ca^{2+}-dependent coupling of ΔSYS. (**F**) HA model representing allosteric interaction of V and Ca^{2+} sensors with channel opening and each other, described by equilibrium constants $L(V)$, $J(V)$, and $K = [Ca^{2+}]/K_d$ and allosteric factors (C, D, and E).

Ca^{2+}-dependent coupling. The activity of mutants was determined over a wide range of voltage and open probability (P_O) in the presence and absence of Ca^{2+}, and the data fit with the HA model to determine gating parameters (C and D) that quantify the allosteric interactions between V and Ca^{2+} sensor activation and channel opening.

Here, we show that while mutations in the S4-S5 linker itself have no appreciable effect on electromechanical coupling, the cytoplasmic ends of S4, S5, and S6 interact to form a noncanonical intrasubunit coupling pathway between VSD and PGD (fig. S1A). This direct pathway involves the apparent rigid-body rotation of S4 and S5 residues about the S5 axis, a "gating lever" that translates S4 movement tangential to the pore axis into S5 rotation, allowing S5 to stabilize the open S6 conformation when V sensors are activated. We also define an indirect pathway mediated by the CTD and C-linker that contributes to both V- and Ca^{2+}-dependent coupling by stabilizing the closed S6 conformation when V and Ca^{2+} sensors are at rest. This pathway proceeds from the VSD to RCK1 and ultimately to S6 through noncovalent interactions of the C-linker with both RCK1 and PGD that bypass the covalent connections between these domains (fig. S1B).

Our results show that both V- and Ca^{2+}-dependent couplings proceed through multiple pathways that are distinct not only in their structural basis but also in their biophysical mechanisms. The VSD apparently acts like a "two-pole switch" that inhibits opening in the resting state and promotes opening in the activated state through direct and indirect coupling pathways involving the TMD and CTD, respectively. Both pathways are mediated by coupling domains (CPDs) within the TMD or CTD that transmit VSD conformational changes to the PGD, probably through rigid-body motions. The indirect pathway also provides insight into the integration of V and Ca^{2+} signaling as it is equally important for V- and Ca^{2+}-dependent coupling and accounts for roughly half the energy of each process. This implies not only that there must be multiple mechanisms linking Ca^{2+} sensor activation to channel opening but also that components of V and Ca^{2+} actions are not independent. Voltage and Ca^{2+} appear to act in a strictly nonadditive manner through the indirect pathway such that activation of V or Ca^{2+} sensors or their simultaneous activation has the same effect, analogous to an electronic open-resting (OR) logic gate, which is fully activated by any combination of active input signals. A gating model incorporating this logic gate–like integration of V and Ca^{2+} by the CTD together with independent action of the remaining V- and Ca^{2+}-dependent coupling pathways can account for both mutant and wild-type (WT) data.

RESULTS

Shortening the C-linker weakens both Ca^{2+}- and V-dependent allosteric coupling

A key feature of BK channels, absent from most K_V channels, is the large CTD. Replacing the CTD of mSlo1 with a short 11-residue tail from K_V1.4 not only abolishes Ca^{2+} sensitivity (*23*) but also reduces the energy of electromechanical coupling by more than half, based

on analysis of ionic and gating currents in the context of the HA model (*18*). While this result is consistent with the hypothesis that the CTD can mediate indirect coupling between VSD and PGD, it also indicates that substantial direct coupling occurs within the TMD in the absence of the CTD and therefore raises questions about the relationship between different electromechanical coupling pathways and their relative contributions. For example, can the effect of CTD removal be entirely attributed to disruption of indirect coupling, or could it also reflect a change in direct coupling due to altered tension on the C-linker and consequent perturbation of the PGD?

The C-linker plays important roles in BK channel gating. It moves laterally relative to the pore upon gating ring expansion and is assumed to be critical for direct transmission of Ca^{2+}-induced conformational changes from CTD to PGD through S6 (*7*). Although the force applied on S6 by the C-linker has not been measured directly, the ability of C-linker deletions and insertions to increase and decrease channel activity, respectively, suggests that the C-linker/CTD complex acts as a passive spring that applies tension on S6 even in the absence of Ca^{2+} to increase channel activity (*24*). Therefore, replacing the CTD could potentially alter tension on S6 and alter direct electromechanical coupling between VSD and S6 if the change is sufficient to perturb S6. To test whether changes in C-linker tension can alter coupling without removing the CTD, the effects on steady-state activation of deleting three residues in the C-linker of mSlo1 were examined (^{335}SYS^{337}; Fig. 1B). This ΔSYS deletion has been shown previously to increase P_O and reduce half-activation voltage ($V_{0.5}$), consistent with the hypothesis that shortening the C-linker increases tension on S6 to promote opening, similar to the proposed action of Ca^{2+} (*24*). Unexpectedly, however, analysis over a wider range of voltage and P_O reveals that ΔSYS has effects on gating distinct from that of Ca^{2+} because it not only increases activity but also substantially weakens both V- and Ca^{2+}-dependent coupling, including a reduction of electromechanical coupling comparable to that of removing the entire CTD (Fig. 1, C to E, and fig. S2, A to E).

A feature of BK channel gating that is critical for allowing allosteric coupling to be measured is that channels can open in the absence of V or Ca^{2+} sensor activation. This is evident from the observation that P_O in 0 Ca^{2+} (5 mM EGTA) achieves a weakly V-dependent "limiting slope" at extreme negative voltages with P_O near 10^{-6} (0 Ca^{2+} WT; Fig. 1C), which can be measured from unitary current activity in macropatches containing hundreds of channels (fig. S2, A and B) and reflects the basal equilibrium constant for the closed-open transition $L(V) = L_0\exp(z_L V/kT)$ (fig. S2D), where $L_0 = L(0)$. The extent to which V or Ca^{2+} sensor activation increases L_0 reflects the strength of sensor/gate coupling, as quantified in the HA model (Fig. 1F) by allosteric factors C and D that represent the fold change in the C-O equilibrium constant induced by activation of Ca^{2+} or V sensors, respectively, in each subunit. Defined in this way, the total fold increase in equilibrium constant by activating Ca^{2+} or V sensors in all four subunits is C^4 or D^4, respectively, and coupling energy is proportional to the logarithm of the allosteric factor [$\Delta G_C = 4kT\ln(C)$, $\Delta G_D = 4kT\ln(D)$]. For WT mSlo1, allosteric interactions are strong such that the C-O equilibrium constant, and hence P_O, increases by more than five orders of magnitude in response to membrane depolarization in 0 Ca^{2+} (Fig. 1, C and E, and fig. S2D) and more than 1000-fold in response to a nearly saturating concentration of Ca^{2+} at negative potentials where V sensors are not activated (Fig. 1E and fig. S2D; 0 versus 70 μM Ca^{2+}), providing independent measures of $D = 17.3$ and $C = 9.1$ (Table 1). The effect of Ca^{2+} is nearly V independent, as evident in Fig. 1C from the similar slope of WT $\log(P_O)$-V relations in 0 and 5.5 μM Ca^{2+} despite a two–order of magnitude increase in P_O. By contrast, ΔSYS in 0 Ca^{2+} produces a greater increase in activity than WT in 5.5 μM Ca^{2+} at negative voltages, but a smaller increase at positive voltages and thus a marked reduction in $\log(P_O)$-V slope compared to the WT curves (Fig. 1C), consistent with a reduction in electromechanical coupling (Fig. 1D and fig. S2E). Mutating the deleted residues individually has virtually no effect (S335A, Y336A, and S337A; Fig. 1, C and D). Thus, shortening the C-linker is sufficient to reduce electromechanical coupling and is not due to disruption of interactions with the deleted residues. Likewise, the increase in P_O at negative voltages from 0 to 70 μM Ca^{2+} is more than an order of magnitude smaller for ΔSYS than WT (arrows, Fig. 1E), consistent with a reduction in Ca^{2+}-dependent coupling. The reduced Ca^{2+} response cannot be accounted for a decrease in Ca^{2+} affinity, as 300 μM Ca^{2+} produced only a slight increase in $\log(P_O)$ relative to 70 μM Ca^{2+} for ΔSYS, consistent with a saturating response (Fig. 1E and fig. S2F). To quantify these effects, the data were fit with the HA model (solid curves, Fig. 1, C and E, and Table 1), indicating that ΔSYS decreases the allosteric factors C and D by 3.0- and 2.6-fold, respectively, while increasing basal activity (L_0) 775-fold.

A potential concern in evaluating electromechanical coupling (D) for ΔSYS, or any mutant that increases channel activity, is that P_O may saturate when V sensors are not fully activated, preventing comparison of the C-O equilibrium $\lambda = P_O/(1 - P_O)$ in the fully activated state (L_V at $V = 0$) to that at rest (L_0). In theory, D can be determined directly from such comparison [i.e., $D^4 = L_V/L_0$, or $D^4 = \lambda(V)/L(V)$ at V sufficient to fully activate VSDs; fig. S2D], similar to approaches based on linkage analysis (*25*, *26*). But, in practice, P_O, which was estimated as G_K/G_{KMAX} in our experiments based on the saturating conductance G_{KMAX} in 70 μM Ca^{2+} (see Materials and Methods), approaches unity with depolarization even in 0 Ca^{2+} for the WT and many mutants, making estimates of L_V noisy or problematic (*26*). In these cases, robust estimates of D can be obtained from HA model fits of the entire $\log(P_O)$-V relation, which are constrained not only by the total change in P_O but also by the shape of the curve (*9*). However, when P_O saturates with voltage, as observed in the presence of Ca^{2+} (Fig. 1C), estimates of D obtained by fitting are not as well constrained as the nonsaturating case and more sensitive to estimates of V sensor charge (z_J), which also affects the slope of the curve (*9*). Therefore, we used an alternative approach ("$q_{\lambda MAX}$ method") to confirm conclusions from fitting by comparing the basal equilibrium constant (L_0) to that where $\lambda(V)$ achieves a maximum logarithmic slope ($q_{\lambda MAX}$) in 0 Ca^{2+}, yielding an estimate of D that is model independent and virtually insensitive to P_O saturation or z_J, provided λ has a symmetrical V dependence (see Supplementary Text). z_J was also estimated on the basis of the above value of D and $q_{\lambda MAX}$, a quantity that can be defined in terms of the HA model as a function of z_J and D (*9*). In the case of ΔSYS, this approach confirmed a substantial (3.0-fold) reduction in D compared to WT, and estimates of D obtained by the $q_{\lambda MAX}$ and fitting methods were highly correlated for all constructs tested ($r = 0.97$, $n = 40$; fig. S2G), supporting conclusions regarding disruption of electromechanical coupling. Estimates of z_J obtained by both methods were also similar to each other and to the WT (fig.

Table 1. HA model parameters for WT and mutant mSlo1. Parameters from HA model fits to mean log(P_O)-V, with V sensor charge (z_J) unconstrained. The V sensor half-activation voltage for closed channels $V_{HC} = -kT\ln(J_0)/z_J$ was derived from z_J, and the V sensor equilibrium constant J_0 at $V = 0$. z_L was determined from the limiting slope of log(P_O)-V at extreme negative voltages $L(V) = L_0\exp(z_L V/kT)$, where L_0 is the basal equilibrium constant for the C-O transition at $V = 0$. Allosteric factors dependent on Ca^{2+} (C and E) were determined by fitting data in 70 μM Ca^{2+} after the other parameters were determined from fits to 0 Ca^{2+} data, with K_d for Ca^{2+} set to the WT value (13.1 μM). When P_O was measured at extreme negative voltages in both 0 and 70 μM Ca^{2+}, C and E were allowed to vary freely, with <C> and SD representing the fit estimate and confidence limit. In cases where P_O at extreme negative voltages was not determined in 70 μM Ca^{2+}, E was set to the WT value (2.8*) and <C> was determined as the average of two HA model fits with and without z_J constrained to 0.58 e. Additional estimates of D and z_J from the $q_{\lambda MAX}$ method are indicated. Mean D (<D>) was determined as the average of the $q_{\lambda MAX}$ estimate and two HA model fits with and without z_J constrained to 0.58 e. Parameters for fits with $z_J = 0.58$ e are in table S1.

	HA model fits								$q_{\lambda MAX}$	Method				
	z_J (e)	z_L (e)	J_0	V_{HC} (mV)	$L_0 \times 10^6$	D	E	C	D	z_J (e)	<D>	SD	<C>	SD
WT	0.64	0.27	0.022	149	1.77	17.2	2.8	9.1	14.8	0.66	17.3	2.58	9.1	0.21
ΔSYS	0.52	0.28	0.043	154	1373	6.7	4.2	3.1	5.0	0.57	5.7	1.17	3.1	0.13
F223A	0.45	0.28	0.248	78	5.85	5.3	1.7	8.8	6.6	0.50	5.5	3.77	8.8	0.46
L224A	0.64	0.32	0.016	163	0.41	17.0	2.8*	8.9	12.7	0.71	16.7	2.99	8.5	1.10
N225A	0.73	0.37	0.036	115	2.29	14.9	2.8*	12.5	17.9	0.71	17.9	3.89	11.7	0.88
I226A	0.73	0.31	0.017	141	0.87	15.6	2.8*	12.7	19.0	0.69	19.4	1.81	11.8	0.23
L227A	0.64	0.31	0.035	133	9.50	14.2	2.8*	9.4	13.3	0.65	14.7	4.54	9.2	0.11
K228A	0.67	0.28	0.020	147	1.30	22.0	4.1	9.7	21.7	0.67	24.5	0.47	9.7	0.25
T229A	0.61	0.26	0.014	179	1.01	16.4	2.8*	9.7	16.8	0.62	16.9	1.28	9.5	0.49
S230A	0.64	0.26	0.015	166	0.35	18.4	2.8*	9.5	18.7	0.63	19.3	1.69	9.2	0.08
N231A	0.71	0.31	0.017	145	1.01	14.4	2.9	8.6	14.2	0.70	15.3	3.44	8.6	0.87
S232A	0.66	0.35	0.026	140	0.76	15.9	2.8*	12.1	11.9	0.72	15.5	1.25	11.4	0.21
V236A	0.56	0.28	0.051	135	3.24	25.4	2.8*	9.4	23.5	0.55	24.0	0.19	9.5	0.08
P320A	0.57	0.21	0.117	95	481	3.7	0.5	5.6	3.4	0.56	3.6	0.64	5.6	0.16
E321A	0.61	0.27	0.068	110	229	7.8	2.9	6.8	7.2	0.64	7.8	1.82	6.8	0.22
I322A	0.62	0.28	0.023	154	3.91	11.9	2.8*	6.5	9.2	0.64	11.3	1.81	6.3	0.14
I323A	0.60	0.28	0.017	173	0.23	23.5	2.8*	7.1	21.3	0.64	23.2	2.18	7.0	0.52
E324A	0.66	0.29	0.029	136	25.8	13.4	2.8*	7.8	12.6	0.65	14.2	2.60	7.4	1.23
L325A	0.71	0.22	0.016	149	0.54	16.6	2.8*	9.9	15.8	0.67	17.7	1.51	9.1	0.36
I326A	0.63	0.28	0.020	157	1.22	17.2	2.8*	8.5	16.3	0.63	17.6	1.10	8.3	0.22
G327A	0.61	0.29	0.019	164	3.81	14.8	2.8*	8.1	13.5	0.63	14.6	3.18	7.9	0.73
N328A	0.64	0.29	0.023	149	0.27	29.7	2.4	17.2	29.4	0.64	31.4	0.07	17.2	0.08
R329A	0.58	0.29	0.028	156	197	8.6	1.8	5.4	8.7	0.57	8.6	0.46	5.4	0.07
K330A	0.63	0.23	0.034	136	41.0	9.2	3.7	5.4	9.3	0.59	9.5	0.89	5.4	0.06
K331A	0.62	0.28	0.021	158	5.25	13.6	6.8	6.1	13.3	0.62	14.0	0.39	6.1	0.08
Y332A	0.58	0.30	0.067	118	287	4.9	4.7	2.6	5.5	0.55	5.1	0.26	2.6	0.03
Y332Q	0.60	0.26	0.076	108	262	5.7	6.1	2.5	5.4	0.62	5.7	1.48	2.5	0.16
G333A	0.60	0.29	0.028	151	2.53	18.1	2.8*	7.9	16.2	0.62	17.8	0.20	7.8	0.04
G334A	0.68	0.27	0.076	96	623	3.8	10.4	2.3	3.8	0.63	3.96	3.06	2.3	0.10
S335A	0.65	0.26	0.019	153	0.88	21.2	5.6	8.4	21.3	0.63	23.0	1.03	8.4	0.06
Y336A	0.59	0.27	0.022	164	2.96	14.1	4.8	5.5	12.5	0.60	13.7	1.49	5.5	0.15
S337A	0.63	0.30	0.023	152	1.11	19.3	6.4	8.4	20.7	06.1	20.8	0.87	8.4	0.04
E386AE388A	0.72	0.34	0.075	91	2.68	15.9	2.8*	15.2	13.8	0.81	16.9	3.73	14.1	1.69
F391A	0.60	0.28	0.024	159	27.8	10.3	4.8	4.2	11.1	0.59	1.7	0.41	4.2	0.04
F395A	0.63	0.27	0.012	176	1.68	16.2	2.9	8.5	18.1	0.60	17.8	1.45	8.5	0.57
F400A	0.57	0.27	0.034	149	35.1	8.3	3.3	3.2	8.4	0.56	8.3	0.11	3.2	0.03
Y401A	0.62	0.29	0.023	153	0.80	22.8	1.4	14.1	22.4	0.63	23.8	2.19	14.1	0.79
Y332AF391A	0.63	0.26	0.057	116	148	4.3	3.9	2.5	4.5	0.57	4.4	0.15	2.5	0.04

continued on next page

	HA model fits								$q_{\lambda MAX}$	Method				
	z_J (e)	z_L (e)	J_0	V_{HC} (mV)	$L_0 \times 10^6$	D	E	C	D	z_J (e)	<D>	SD	<C>	SD
Y332AF400A	0.49	0.29	0.051	153	165	6.9	2.5	2.8	6.7	0.51	6.5	0.58	2.8	0.04
F391AF400A	0.50	0.28	0.032	176	582	5.9	4.6	2.0	4.9	0.52	5.2	0.64	2.0	0.02

S2H), averaging 0.62 ± 0.06 *e* (mean ± SD) by both approaches, consistent with the expectation that charge should not be altered as, aside from three uncharged residues at the C terminus of S4, all sites mutated were outside of the VSD, and removal of the entire CTD has no effect on z_J measured with gating current (*18*). That said, variability in estimation of z_J can contribute to variability in *D* by fitting. Therefore, *D* was ultimately determined throughout this study as the average of three estimates: the $q_{\lambda MAX}$ method and two HA model fits with and without z_J fixed to the WT value measured from gating current (0.58 *e*; Table 1 and table S1) (*12*). This approach yielded standard deviations in *D* that are larger than any individual method, but better reflects the potential sources of error and uncertainty in quantifying electromechanical coupling.

How does ΔSYS perturb electromechanical coupling? Although the C-linker has an extended structure (fig. S1A), comparison of apo and Ca^{2+}-bound Slo1 structures indicates that the C-linker moves without change in length, suggesting that it does not itself behave as spring (*7*). Therefore, shortening the C-linker could potentially perturb coupling by increasing tension on S6 or the CTD, or by altering the position of these regions or the C-linker to disrupt their interaction with sites distal to the deletion. If specific interactions are disrupted, then point mutations at interaction sites may reproduce the effect of ΔSYS without shortening the C-linker. To test this possibility, effects of individual Ala substitutions in multiple domains including S4-S5 linker, S6, C-linker, and RCK1 domain were investigated.

S4-S5 linker mutations perturb opening but not electromechanical coupling

Because the S4-S5 linker is considered essential for electromechanical coupling in K_V channels, an Ala scan was first performed in the S4-S5 linker region, including the last helical turn of S4, S4-S5 linker, and two turns of S5 (Q222 to V236 in mSlo1; Fig. 2A). Although the linker is a short loop of four amino acids that does not contact S6 in hSlo1 structures (Fig. 2B), there are several ways in which this region could potentially participate in electromechanical coupling. First, it is conceivable that the linker interacts with S6 in a different conformational state, as only two states are represented by existing structures and questions remain whether the PGD in the "Ca^{2+}-free closed" structure is fully closed and whether the VSD in the "Ca^{2+}-bound open" structure (which also has Mg^{2+} bound) is fully activated (*16*). Second, the S4-S5 linker region contacts the CTD (*7*) and represents the only resolved noncovalent interaction between VSD and CTD in the Ca^{2+}-free hSlo1 structure, suggesting a role in indirect coupling (*17*). Last, owing to the nonswapped architecture of Slo1, contacts exist between the bottoms of S4, S5, and S6 within each subunit (Fig. 2B, left side), which could potentially couple VSD to PGD, independent of the S4-S5 linker. Consistent with these possibilities, most mutations in the S4-S5 linker region perturbed the half activation voltage ($V_{0.5}$) of macroscopic G_K-*V* relations in 0 Ca^{2+} or 70 μM Ca^{2+} (Fig. 2C), and most were harder to activate than the WT ($\Delta V_{0.5} > 0$). $V_{0.5}$ for several mutations in S4 (Q222A) and S5 (I233A, K234A, L235A) shifted positive by more than 50 mV in 70 μM Ca^{2+} and could not be measured in 0 Ca^{2+}. However, the S4-S5 linker shows a somewhat different pattern, with two mutations having little or no effect (I226A and K228A) and two shifting to more negative voltages (N225A and L227A). V236A in S5 also produced a negative shift, and F223A in S4 was unique in shifting $V_{0.5}$ in opposite directions in 0 and 70 μM Ca^{2+}.

Despite extensive perturbation of $V_{0.5}$ by S4-S5 linker region mutations, analysis of log(P_O)-*V* relations in 0 Ca^{2+} indicated that changes in electromechanical coupling were limited and did not involve the S4-S5 linker, with only F223A in S4 showing a clear reduction in *D* factor (Fig. 2, D and E). Instead, most mutations simply altered the basal C-O equilibrium constant (L_0; Fig. 2F and Table 1), as illustrated in fig. S3A by several examples that increase (L227A) or decrease (L224A, S230A) P_o by ~3-fold relative to the WT, without appreciably changing the shape of the log(P_O)-*V* curve. Similarly, V236A in S5 shifts the log(P_O)-*V* relation to more negative voltages without change in shape (fig. S3B), consistent with an increase in the voltage sensor equilibrium constant (J_0) without change in coupling.

Mutations producing the greatest increases in $V_{0.5}$ (Q222A, I233A, K234A, and L235A) reduced activity to such an extent that complete log(P_O)-*V* relations could not be determined in 0 Ca^{2+} and *D* could not be estimated. However, evidence suggests that they all suppress basal activity and therefore are linked in some manner to pore opening. While the mutants exhibited maximal conductance in 70 μM Ca^{2+} comparable to WT, indicating normal expression, P_O in 0 Ca^{2+} remained below 0.1 at the highest voltages tested (fig. S3, C and D), and no activity could be detected in the same patches at negative voltages in 0 Ca^{2+}, implying that L_0 is reduced below our detection limit (~10^{-7}) and therefore at least 10-fold lower than the WT. Consistent with this conclusion, limiting P_O at negative voltages in 70 μM Ca^{2+} was 42- to 174-fold lower than the WT. While the latter could conceivably be due to a reduction in Ca^{2+}-dependent coupling (*C* factor), this appears unlikely as at $V_{0.5}$ in 70 μM Ca^{2+} switching to 0 Ca^{2+} produced large (>500-fold) decreases in macroscopic current, consistent with normal Ca^{2+} sensitivity (fig. S3D), and the reduction in limiting P_O from 70 to 5.5 μM Ca^{2+} for Q222A (33 ± 3–fold) was consistent with the WT (29 ± 6–fold; fig. S2E, arrows). Estimated values of L_0 for these mutants, based on 70 μM Ca^{2+} data and assuming a normal *C* factor, are shown in Fig. 2F (red bars).

A gating lever mediates electromechanical coupling in the TMD

Among mutations in the S4-S5 linker region, F223A stands out as it reduces electromechanical coupling to a similar extent as ΔSYS.

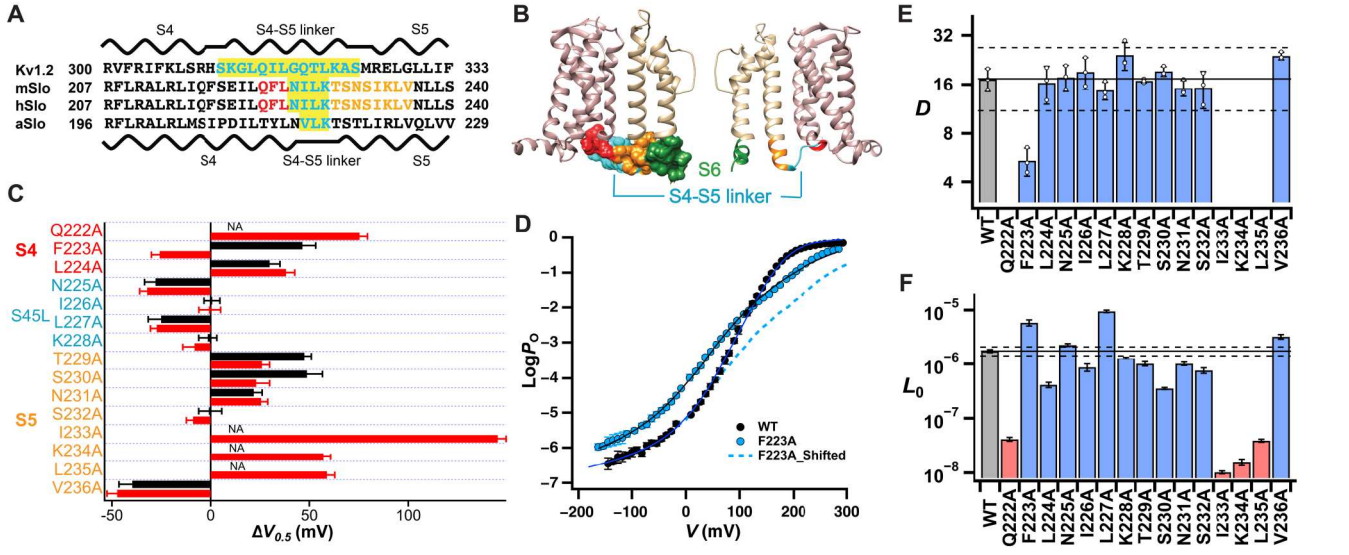

Fig. 2. Ala scan of S4-S5 linker region. (**A**) Sequence alignment with secondary structure showing that the S4-S5 linker (highlighted in yellow) is much larger in $K_V1.2$ than in Slo1. Colored text indicates residues mutated in mSlo1. (**B**) TMD structure of apo hSlo1 highlighting the relationships between the S6 tail (green), S4-S5 linker (blue), and regions mutated at the bottom of S4 (red) and S5 (orange). (**C**) Differences in $V_{0.5}$ between Ala mutants and WT mSlo1 in 0 Ca^{2+} (black) and 70 μM Ca^{2+} (red). (**D**) Mean log(P_O)-V of F223A and WT in 0 Ca^{2+}. Solid curves are HA model fits. Dashed curve is F223A data superimposed on the foot of the WT curve to highlight the reduction in V-dependent activation. (**E** and **F**) Allosteric factor D and basal activity L_0 for WT and mutants in 0 Ca^{2+}. For Q222A, I233A, K234A, and L235A, P_O was too low in 0 Ca^{2+} to measure $V_{0.5}$, D, or L_0, but L_0 was estimated (red bars) from basal activity in 70 μM Ca^{2+}.

However, the mechanisms of F223A and ΔSYS action differ, suggesting that they involve different pathways. First, unlike ΔSYS, F223A has no effect on Ca^{2+}-dependent coupling (fig. S3F and Table 1), suggesting that its action is confined to the TMD. Second, while ΔSYS increases L_0 by almost three orders of magnitude (Table 1), F223A produces only a 3.3-fold increase in P_O at negative voltages (L_0) and a decrease at positive voltages (L_V) that together result in a greatly reduced V-dependent change in P_O, which is most evident when log(P_O)-V relations for WT and F223A are superimposed at negative voltages (Fig. 2D, dashed curve). The gradual increase in P_O for F223A observed at more positive voltages is consistent with the expectation, reflected by the HA model fit, that if L_V is reduced such that P_O does not saturate, then P_O will still increase according to the intrinsic V dependence of the C-O transition (z_L). The 3.3-fold increase in L_0 and the 3.15-fold decrease in D produced by F223A indicate that L_V is reduced 30-fold ($\Delta L_V = \Delta D^4/\Delta L_0$), implying that F223 normally helps promote opening when V sensors are activated.

The interaction pathway underlying a role of F223 in electromechanical coupling is not immediately obvious as its side chain faces away from the PGD. Similarly, E219 in S4, one helical turn above F223, faces away from the pore but has been implicated in electromechanical coupling as well as a functional interaction with E321 in S6 (*27*). A likely explanation for the role of these residues and F223 is revealed by the sensitivity to mutation of intervening residues (Q222, I233, K234, and L235), which provide a continuous pathway linking F223 (S4) to E321 (S6) through the cytoplasmic ends of S4, S5, and S6 (Fig. 3A). Mutations of these residues strongly reduce L_0 (Fig. 2F), suggesting that they normally help stabilize the open conformation. Why this is the case, and how S4-S5 residues form a pathway for coupling VSD to PGD, can be seen by comparing the apo closed and Ca^{2+}-bound open structures of hSlo1, which are also thought to have resting and activated VSDs, respectively. During opening, S6 bends and moves toward S5, enhancing contact between the bottom of S5 and S6. In the closed structure, among the above residues, only K234 in S5 contacts S6 (I322; Fig. 3B). However, in the open structure, both K234 and L235 contact multiple residues in S6, including a salt-bridge interaction between K234 and E321 (N-O distance, 3.57 Å), explaining why K234 and L235 help stabilize the open conformation (Fig. 3C). This interaction depends not only on the bending of S6 upon PGD opening but also on a rotation of S5 that is apparently associated with VSD activation (Fig. 3D). The S5 helix and selectivity filter of the two structures are superimposable, indicating that there is no lateral movement of S5 relative to the pore axis during activation that could contribute to stabilization of the open S6 conformation. However, K234 and L235 rotate together with S5 by ~20°, sufficient to move these side chains by several angstroms relative to their S6 interaction partners and stabilize the open state. On the basis of the superimposed structures, the rotation of S5 is necessary for K234 to contact S6 in the open conformation (fig. S4A). S5 rotation is associated with an apparent rigid-body rotation of a cluster of S4 and S5 residues (Fig. 3D and fig. S4B). We call the core of this cluster, formed by F223, Q222, I233, K234, and L235, the gating lever. That rotation of the gating lever and S4 movement contributes to open state stabilization is supported by the observation that Q222 and I233 at the S4/S5 interface maintain a constant relationship (fig. S4B) and mutating them reduces L_0, suggesting that they interact strongly and their interaction is important for opening. A number of additional residues in the bottom of S5 and S4-S5 linker that are less sensitive to mutation rotate with the gating lever, suggesting that they might also contribute to gating lever structure (e.g., through their backbone), and that the motion is transmitted to the VSD/CTD interface.

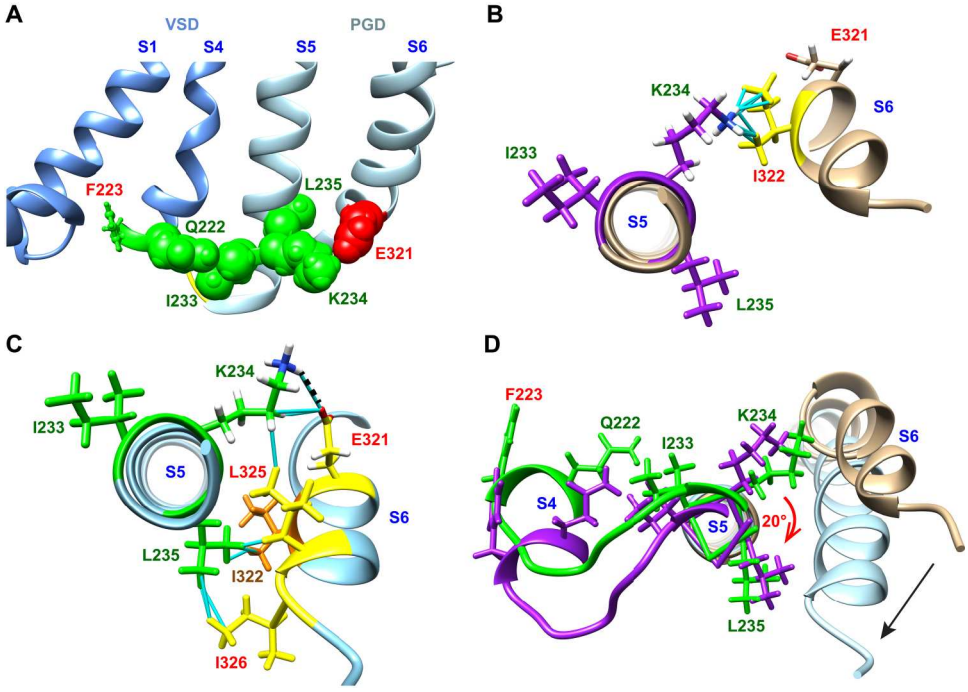

Fig. 3. Electromechanical coupling mechanism in the TMD. (**A**) Gating lever (green) provides a pathway connecting F223 (S4) and E321 (S6) in the open, Ca^{2+}-bound hSlo1 structure (6V38). (**B**) Apo closed structure viewed from the cytoplasmic side of the channel shows minimal contact between gating lever residues (purple) and S6. (**C**) In the Ca^{2+}-bound open structure, gating lever residues K234 and L235 make extensive contact with S6 (E321, I322, L325, and I326), including a salt-bridge interaction between K234 and E321 (dashed line). (**D**) Changes in S5/S6 interaction and F223 movement are associated with rigid-body rotation of the gating lever and S5 by ~20° (purple: apo closed; green: Ca^{2+}-bound open). Structures were aligned to S5 through the N-terminal end of S6.

Rotation of the gating lever is linked with movement of S4 and F223, suggesting that it is driven by VSD activation and plays a role in electromechanical coupling. At one end of the gating lever, S5 rotation is important for engaging S6 and stabilizing the open PGD conformation. At the other end, F223 changes its relationship to other VSD residues and therefore may form interactions that depend on the state of VSD activation. For example, F223 contacts S1 (A107 and R113) in the apo resting state (fig. S4C), but not in the Ca^{2+}-bound activated state. Disruption of these VSD interactions by F223A could potentially destabilize the closed-resting (CR) state, consistent with the ability of this mutation to increase both L_0 and the equilibrium constant for VSD activation J_0 (Table 1). F223 also interacts with K392 in the CTD in the Ca^{2+}-bound but not the apo structure. However, why F223A reduces L_V in 0 Ca^{2+} (i.e., destabilizes the open-activated state) is unclear, in part, because the structure of the apo open conformation is unknown. In any case, a dependence of gating lever interactions on both PGD opening and VSD activation can account for a role of F223 in electromechanical coupling and suggests that other residues in this pathway (e.g., K234) might also contribute, although the effects of Ala substitutions at these positions were too extreme to allow coupling to be quantified.

A key assumption of the proposed mechanism is that the movement of S4 and gating lever rotation is driven by V sensor activation rather than gating ring expansion. This cannot be confirmed by comparing apo and Ca^{2+}-bound structures, which differ in both VSD and gating ring conformation, but it is consistent with the role of F223 in electromechanical coupling and additional analysis below. Under the conditions used to determine Ca^{2+}-bound structures (saturating Ca^{2+} and Mg^{2+}, $V = 0$), hSlo1 achieves maximal P_O (*28*) and therefore is expected to have activated V sensors, owing to the bidirectional nature of allosteric coupling. That is, opening favors V sensor activation, consistent with the observation that steady-state Q-V and P_O-V curves for mSlo1 are superimposable in saturating Ca^{2+} (*12*). The large conformational change in S6 suggests that Ca^{2+}-bound structures are indeed open. The VSD also undergoes conformational changes, including movement of S4 toward the extracellular direction and S1-S3 in the opposite direction, that are small (1 to 2 Å; fig. S4D), and possibly beyond structural resolution, but qualitatively consistent with the reported contribution of basic R213 (S4) and acidic residues D153 (S2) and D186 (S3) to gating charge (*9*). However, the largest conformational change in the VSD is the movement of the bottom of S4 tangential to the pore axis by more than 6 Å (Fig. 3D), which involves a bending of S4 below R213. We hypothesize that it may be driven by a combination of subtle vertical movement of VSD helices relative to each other and S5, and consequent changes in interaction among segments. That V sensor activation is sufficient to alter S4/S5 interaction is supported by the ability of an S5 mutation in this interface, V236A, to facilitate V sensor activation (fig. S3B and Table 1). In addition, changes in contact between the bottom of S4 and S1 are observed in the Ca^{2+}-bound structure that would tend to stabilize the bent S4 conformation, including an increase in buried solvent-accessible surface area of ~30% and changes in specific side-chain interactions. For example, F217 (S4) contacts V236 (S5) in the apo structure but moves to form a potentially favorable stacking interaction with F120 (S1) in the Ca^{2+}-bound conformation (fig. S4D). Two lines of evidence argue against the alternative

hypothesis that gating ring expansion drives S4 movement and gating lever rotation. First, while Ca^{2+} binding causes the αB segment of RCK1 to move laterally outward and up toward the VSD where it contacts the bottom of S4 and S4-S5 linker, the bending of S4 is toward rather than away from this contact, suggesting that it is not produced by the CTD simply "pushing" on S4. Second, if interactions between αB and VSD produced by gating ring expansion drive gating lever rotation to promote opening, then this pathway should contribute to Ca^{2+}-dependent coupling. However, mutation of F223 (S4), or N225 or K228 in the S4-S5 linker, which contact αB in the Ca^{2+}-bound but not the apo structure, have no appreciable effect on Ca^{2+}-dependent coupling (figs. S3F and S4E and Table 1).

Pro and Gly "hinges" in S6 and the C-linker influence electromechanical coupling

To determine the contribution of S6 and C-linker residues to electromechanical coupling, an Ala scan was performed between the inner pore and SYS deletion site (P320→G334 in mSlo1), including regions near the gating lever. The sequences of mSlo1 and hSlo1 are identical in this region (Fig. 4A). S6 in hSlo1 is mostly α-helical and transitions to an extended structure at G327, where the pore ends and the C-linker begins. S6 and the C-linker bend at various "hinge" locations during gating as defined by a proline in S6 (P320) and two unusual di-glycine motifs G310/G311 and G333/G334, the latter of which is highly conserved in Slo1 and Slo2 (Fig. 4, A and B, and fig. S5). In K_V channels, S6 forms an intracellular gate at the "PVP" bundle crossing (*29*). hSlo1 lacks an S6 bundle crossing (Fig. 4B), and closing of the PGD in BK channels has been proposed to involve either a conformational change in the selectivity filter (*30*, *31*) or a hydrophobic dewetting transition in the pore (*32*). However, in either case, movement of the pore-lining S6 helix, which is similar in magnitude to that predicted for $K_V1.2$ (fig. S5A), is thought to couple conformational changes in V and Ca^{2+} sensors to the gate. Thus, mutations in S6 or the C-linker could potentially reduce coupling by directly disrupting interactions between mutated residues and the VSD or CTD, or by altering the orientation and flexibility of these regions in such a way that their interaction with other domains is perturbed or not transmitted efficiently to the gate.

Within the intracellular end of S6 (P320-I326), a marked decrease in electromechanical coupling (*D*) was observed upon mutating P320, and to a lesser extent E321 and I322 (Fig. 4C). The latter are consistent with the proposed gating lever mechanism in that E321 and I322 contact S5 residues K234 and I235 in a state-dependent manner (Fig. 3, B and C), and the sum of the energetic effects of E321A and I322A on *D* ($\Delta G_D = 2.92 \pm 0.40$ kcal/mol) is similar to that of F223A (2.84 ± 0.48 kcal/mol), suggesting that they may represent two ends of the same pathway. By contrast, the effect of P320A on coupling likely reflects a structural perturbation, as the Pro side chain does not contact other transmembrane segments, but removal of Pro from kinked helices often reduce or eliminate bends (*33*), which could disrupt interaction of downstream residues including E321 and I322. Likewise, the ability of G334A at the other end of the scanned region to reduce *D* to a similar extent as P320A or ΔSYS (Fig. 4, C and D) probably involves a structural perturbation as the C-linker bends at this position (fig. S5C) such that an Ala side-chain substitution is expected to clash with the backbone of neighboring residues (G333 and S335; fig. S5D), forcing a change in backbone angle. Whether this change could disrupt coupling through perturbation of local or distal interactions is uncertain. The G334 backbone forms a hydrogen bond with R413 in RCK1

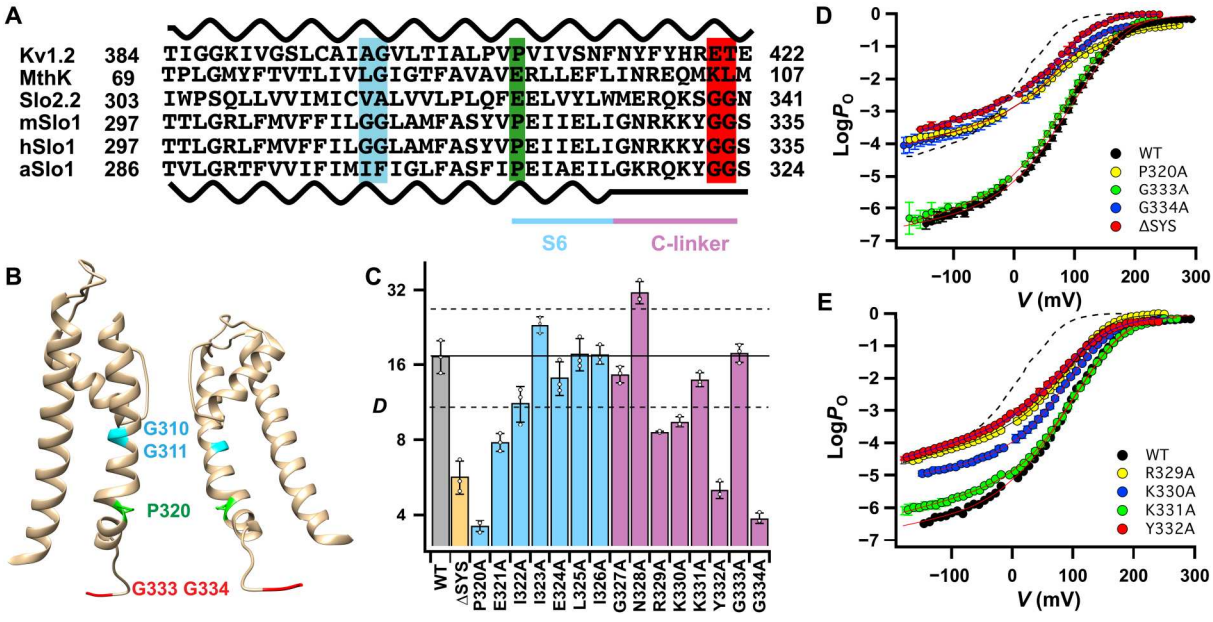

Fig. 4. Ala scan of S6 and C-linker. (**A**) Sequence alignment for $K_V1.2$, MthK, and Slo channels, with conserved hinge residues highlighted, secondary structure indicated for $K_V1.1$ (top) and Slo1 (bottom), and regions mutated indicated by colored bars. (**B**) Position of hinge residues is indicated in apo hSlo1 structure. (**C**) Allosteric coupling factor *D* for mutants in S6 and C-linker compared to WT and ΔSYS, with dashed lines indicating 3 SDs from WT mean. Mean log(P_O)-*V* relations in 0 Ca^{2+} for (**D**) WT and hinge mutations (P320A, G333A, G334A, and ΔSYS) or (**E**) C-linker mutations (R329A, K330A, K331A, and Y332A). Solid curves are HA model fits. Dashed curve is WT mean data in 5.5 μM Ca^{2+}.

(fig. S5D), which could potentially be disrupted by changes in backbone angle. However, R413 is relatively far (~20 Å) from the VSD/CTD interface (fig. S1B), providing no clear pathway for electromechanical coupling. As discussed later, we suggest that the effects of G334A and ΔSYS are related to the mechanism proposed below for the nearby C-linker mutation Y332A.

Role of Y332 in the C-linker in electromechanical coupling

Aside from G334A, several mutations in the C-linker (G327-G334) weakened electromechanical coupling, most notably Y332A, and to a lesser extent R329A and K330A (Fig. 4C). The latter are contained within a cluster of three positively charged residues (^{329}RKK^{331}), the "RKK ring" that surrounds the inner mouth of the pore. These residues are proposed to be important for stabilizing the closed conformation as a result of intersubunit interactions with negatively charged residues (E321 and E324) in S6 and strongly perturb the closed-open equilibrium when mutated simultaneously (*34*). However, individual mutations at these sites had more modest effects, with R329A and K330A each producing 30- to 100-fold increases in L_0 together with approximate twofold reductions in electromechanical coupling (D; Table 1 and Fig. 4E). A greater effect was observed for Y332A, which reduced D 4.1-fold while increasing L_0 more than 100-fold. This residue also stood out as adjacent mutations (K331A and G333A) had little effect (Fig. 4, C to E), consistent with a localized interaction, and because Y332 is the first residue in the C-linker to make extensive contact with the CTD.

Interaction of Y332 with F391 and F400 in RCK1 mediates electromechanical coupling

On the basis of Slo1 structure, neither the RKK ring nor Y332 interacts directly with the VSD. However, Y332 faces a loop formed by αB and βC segments ("αB-βC loop," N384-Y401) of RCK1 in the same subunit, and αB, in turn, contacts the VSD of an adjacent subunit (*7*), suggesting that a pathway could exist for coupling the VSD to the PGD through Y332. To test this hypothesis and identify interaction partners for Y332, the effects of select Ala substitutions in the αB-βC loop were determined. Because this region is rich in aromatic residues that potentially contact or interact at distance with Y332 through π-π aromatic-aromatic interactions, these residues were primarily targeted (F391A, F395A, F400A, and Y401A), together with a double mutation (E386A/E388A), as E388 contacts Y332 and forms a salt bridge with the adjacent C-linker residue (K331) in the Ca^{2+}-bound structure, whereas E386 contacts S5. Among these mutations, only F391A and F400A reduced electromechanical coupling (Fig. 5, A and B), suggesting that F391 and F400 may be interaction partners for Y332.

In hSlo1, F391 in αB and F400 in βC are close enough to Y332 and to each other to interact, and F400 contacts Y332 and F391 (Fig. 5C). However, whether these interactions occur or contribute to coupling is difficult to predict a priori, especially as aromatic-aromatic interactions can have strong geometric requirements and be attractive or repulsive depending on side-chain orientation and distance (*35*, *36*). To determine whether perturbations in coupling by mutations at Y332, F391, and F400 reflect interactions among these residues, we analyzed the effects of double mutations for each pair (Y332A/F391A, Y332A/F400A, and F391A/F400A; Fig. 5, A, D, and E). The results confirm that interactions of Y332 with both F391 and F400 (but not F391 with F400) contribute to electromechanical coupling and basal activity.

If two residues interact to mediate allosteric coupling, then the effects on coupling energy of mutating the residues should be nonadditive (*37*). This is clearly the case for Y332 and its interactions with F391 and F400, as the double mutants Y332A/F391A and Y332A/F400A have effects on $\log(P_O)$-V in 0 Ca^{2+} (Fig. 5D) and coupling (Fig. 5A) similar to Y332A alone. This implies not only that Y332 interacts with both F391 and F400 but also that the Ala substitution at Y332 is sufficient to completely disrupt these interactions. Although the nature of the interaction was not studied in detail, Y332Q disrupted coupling to the same extent as Y332A (Fig. 5A), which is consistent with a π-π aromatic-aromatic interaction, as is the apparent lack of direct contact between Y332 and F391 (Fig. 5C). By contrast, the effects of F391A and F400A on coupling are energetically additive, implying that any interaction between F391 and F400 does not contribute to coupling. This was quantified using double-mutant cycle analysis to determine an interaction parameter $\Omega(A,B) = \Delta G(AB) + \Delta G(WT) - \Delta G(A) - \Delta G(B)$, based on electromechanical coupling energy (ΔG_D) for single and double mutations at sites A and B (Fig. 5E). The result for F391A/F400 is close to zero (Ω = 0.01 ± 0.69 kcal/mol, mean ± SD) indicating an additive effect, whereas those for Y332A/F400A (Ω = 2.34 ± 0.68 kcal/mol) and Y332A/F391A (Ω = 0.83 ± 0.66 kcal/mol) suggest that Y332 interacts more strongly with F400 than F391, consistent with their relative proximity. The energetic change in basal activity (L_0) produced by these mutations exhibits a similar pattern but with smaller error (Fig. 5E), further supporting that Y332 interacts with both F391 and F400. Last, it is notable that the effect of F391A/F400A is similar to Y332A (Fig. 5, A and D), implying that these residues form a self-contained network. That is, the effects of mutating Y332, F391, or F400 can be accounted for by disruption of the interactions between them without the need to postulate the existence of additional interactions with other residues.

The YFF pathway acts by suppressing activity of resting states

Electromechanical coupling can potentially act to enhance channel activity when V sensors are activated (L_V) and/or suppress activity at rest (L_0). However, the pathway that depends on interaction of Y332 with F391 and F400 ("YFF pathway") appears to act exclusively by the latter mechanism. This is evident, qualitatively, from the observation that Y332A and related mutations that disrupt this pathway increase P_O in 0 Ca^{2+} at negative voltages (L_0), with little impact at depolarized voltages (Fig. 5, B and D), and quantitatively by comparing the relationship between L_0 and D (Fig. 6A). If a mutation disrupts coupling solely by relieving suppression of L_0, with no effect on L_V, then the changes in D and L_0 should follow an inverse fourth power relationship (red line, Fig. 6A), which appears to be the case for many mutations tested, including those involving Y332, F391 or F400 (red symbols), and G334A.

The YFF pathway also mediates Ca^{2+}-dependent coupling

The importance of Y332/αB-βC loop interaction for electromechanical coupling suggests that the YFF pathway might also contribute to Ca^{2+}-dependent coupling, as the αB-βC loop moves over 12 Å away from the pore axis in response to Ca^{2+} binding. Despite this large displacement, the structure of the αB-βC loop and relative positions of Y332, F391, and F400 in apo and Ca^{2+}-bound hSlo1 remain virtually constant (Fig. 5C), implying that the interaction of Y332 with F391 and F400 is strong and acts to anchor Y332

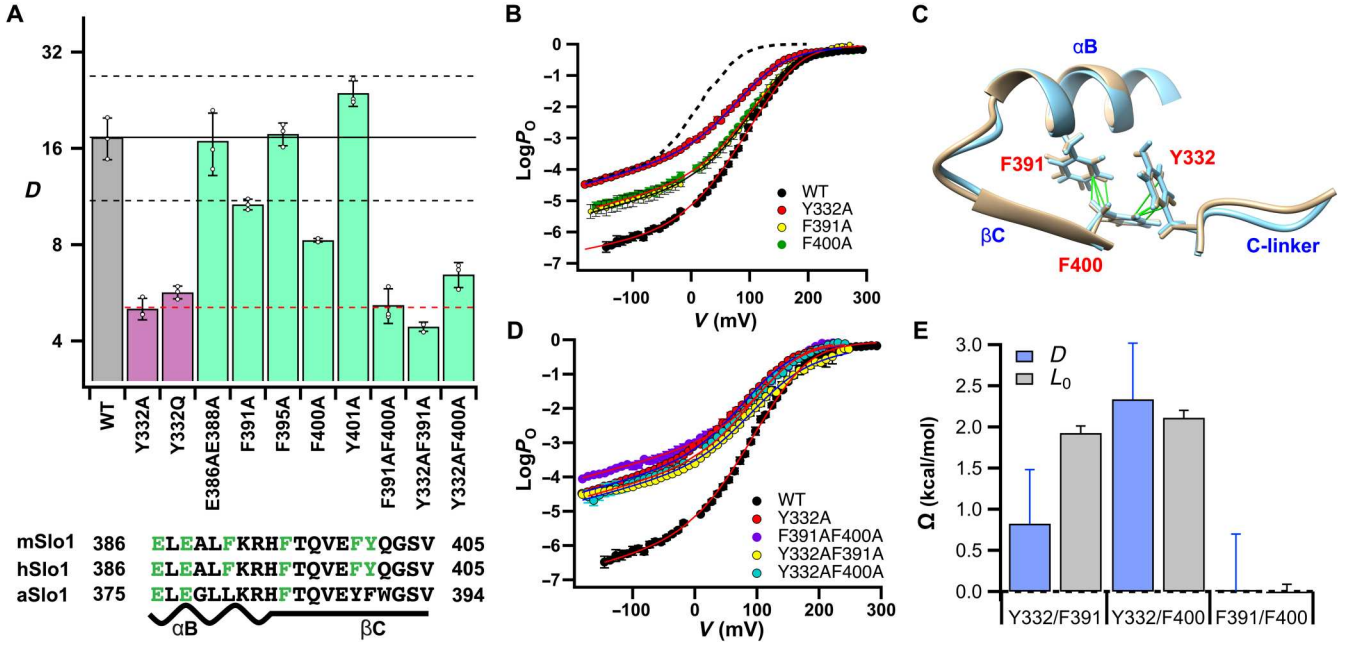

Fig. 5. Ala scan for Y332 interaction partners. (**A**) Allosteric coupling factor *D* for mutants in Y332 or αB-βC loop of RCK1. Sequence alignment for Slo1 orthologs with mutated positions in green. (**B**) Mean log(P_O)-*V* relations for F391A, F400A, Y332A, and WT in 0 Ca^{2+}. Solid curves are HA model fits; dashed curve is WT 5.5 μM Ca^{2+}. (**C**) Structure of αB-βC loop showing proximity of Y332 with potential interaction partners F391 and F400. Apo (tan) and Ca^{2+}-bound (blue) structures are superimposable. Contacts are shown for apo structure. (**D**) Mean log(P_O)-*V* relations in 0 Ca^{2+} for WT, Y332A, Y332A/F391A, Y332A/F400A, and F391A/F400A, showing similarity between double mutants and Y332A. Solid curves are HA model fits. (**E**) Double-mutant cycle analysis showing that interaction of Y332 with both F391 and F400 (but not F391 with F400) contributes to changes in *D* (blue) and L_0 (gray) based on the apparent interaction energy (Ω) determined for these parameters, as described in the text.

and the C-linker to the αB-βC loop during gating ring expansion. To test the prediction that disruption of these interactions may inhibit Ca^{2+}-dependent activation, the allosteric factor *C* was determined for most mutants that alter *D* by measuring the increase in P_o from 0 to 70 μM Ca^{2+} at extreme negative voltages as in Fig. 1E and, in other cases, by fitting macroscopic 70 μM Ca^{2+} data to the HA model. *C* was calculated on the basis of the simplifying assumption that the Ca^{2+}-binding affinity of the closed channel (K_{dC}) is the same as WT (13.1 μM). This is a reasonable approximation provided that 70 μM Ca^{2+} is a nearly saturating concentration, which was confirmed for most mutants that alter *C* by verifying that the change in limiting P_O from 70 to 300 μM Ca^{2+} is small (fig. S2F). The results show that many mutations near Y332 reduce *C* (Fig. 6B) and reveal an inverse fourth power relationship between changes in L_0 and *C*, for mutations involving Y332, F391 or F400 (red), and G334A, implying that these mutations relieve suppression of L_0, with no effect on the C-O equilibrium when Ca^{2+} sensors are fully activated (L_{Ca}).

The YFF pathway acts as a molecular logic gate for V- and Ca^{2+}-dependent coupling

That interaction of Y332 with F391 and F400 contributes to both V- and Ca^{2+}-dependent coupling suggests that the αB-βC loop moves with V and Ca^{2+} sensor activation and regulates channel activity through the C-linker. Because Ca^{2+} and voltage have nearly additive effects on BK channel activity under many conditions (*12*, *22*) and gating ring expansion is proposed to enhance activity by pulling S6 open (*7*, *24*), one might suppose that V and Ca^{2+} sensor activation produce additive increases in activity by pulling the αB-βC loop in different directions. However, the effects of mutation are inconsistent with such a mechanism, indicating instead that the YFF pathway acts to suppress activity when V and Ca^{2+} sensors are at rest rather than promote activity when sensors are activated. Moreover, as discussed below, these results indicate that the effects of Ca^{2+} and V are strictly nonadditive such that activation of either V or Ca^{2+} sensor is sufficient to exert maximal effect, analogous to the function of a digital logic gate.

The effects of V- and Ca^{2+}-dependent coupling on channel activity can be understood in terms of a thermodynamic cycle (Fig. 6C) representing the equilibrium constant for the C-O transition (at $V = 0$) as it increases from its basal level L_0 to L_V or L_{Ca} upon activation of V or Ca^{2+} sensors, respectively, and to $L_{Ca,V}$ when both sensors are activated. The changes in equilibrium free energy between these states represent coupling energies (e.g., ΔG_D and ΔG_{CD} represent electromechanical coupling in 0 and saturating Ca^{2+}, respectively). For simplicity, we assume that this cycle represents the contribution of the YFF pathway alone, in the absence of other coupling mechanisms. As noted above, relationships between L_0 and *D* or *C* for mutant and WT channels (Fig. 6, A and B) imply that disruptions in coupling by mutating the YFF pathway are fully accounted by changes in L_0, leaving L_V and L_{Ca} unchanged. These conclusions have important implications for the relationship between V- and Ca^{2+}-dependent coupling. First, if perturbations in *C* and *D* are both accounted for by changes in L_0, then they must be energetically equal. Plotting *C* versus *D* shows that this is indeed the case for mutations near Y332, which produce approximately equal fractional changes in these parameters relative to the WT (Fig. 6D, red lines), unlike mutations in the TMD (e.g., F223A, E321A, and P320), which primarily perturb electromechanical

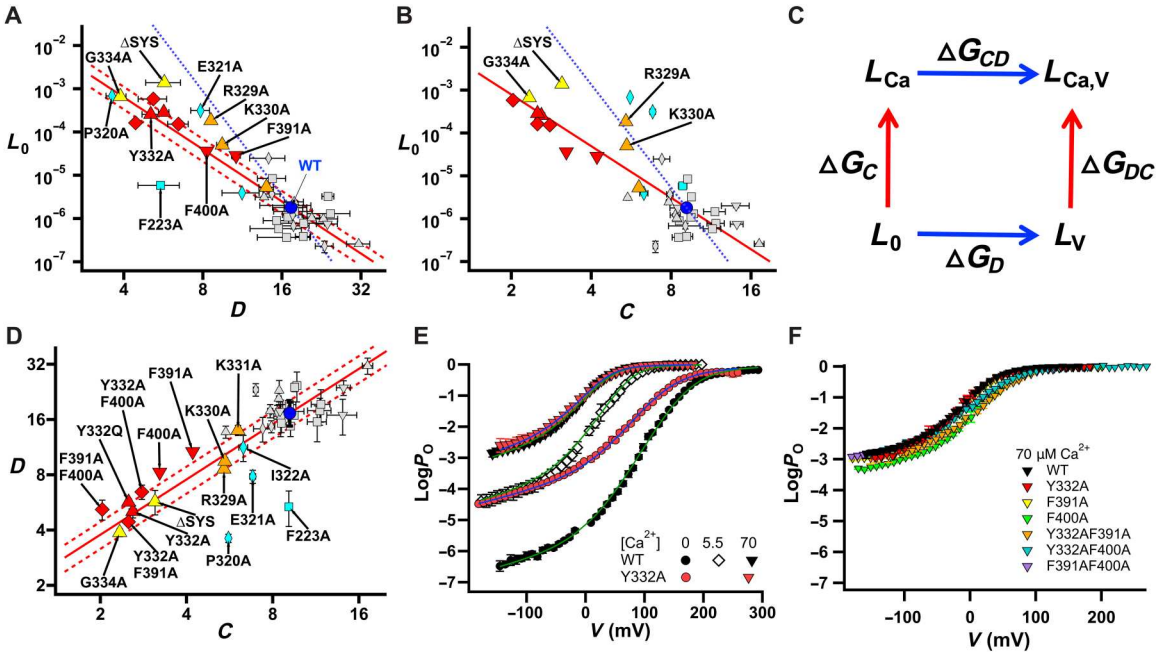

Fig. 6. The YFF pathway mediates V- and Ca^{2+}-dependent coupling by suppressing resting activity. (**A** and **B**) Plots of basal activity (L_0) versus allosteric coupling factor *D* or *C* for all constructs tested. Red and blue lines represent inverse fourth and eighth power relations between L_0 and coupling factor [e.g., L_0(mut) = L_0(WT)(D_{WT}/D_{Mut})^n, where n = 4 or 8]. Symbols indicate mutation location, S4-S5 linker region (■), S6 (♦), C-linker (▲), or αB-βC loop (▼) and double mutants involving Y332, F391, and F400 (◆). Colors indicate mutants involving Y332, F391, and F400 (red), RKK ring (orange), and G334A or ΔSYS (yellow) and mutants in the TMD that alter coupling (P320, E321A, I322A, and F223A) (blue), with all others being gray. (**C**) Thermodynamic cycle showing C-O equilibrium constant as it increases from basal level L_0 to L_V or L_{Ca} when all V or Ca^{2+} sensors are activated or $L_{Ca,V}$ when both sensors are activated. Δ*G* values represent energy change between states. (**D**) Plot of coupling factors *D* versus *C*. Solid line represents equal energetic change in both parameters relative to WT; dashed lines reflect ±SD of the WT value of *D*. (**E**) Mean log(P_O)-*V* relations for WT and Y332A. Solid curves are fits to Scheme 1b with z_J = 0.58, z_L = 0.28, V_{HC} = 117.2 mV, J' = 0.068, L' = 2.47 × 10^{-4}, K'_D = 4.83 μM, C' = 2.44, D' = 5.22, E' = 4.58 (Y332A: Y_1 = Y_2 = 1; WT: Y_1 = 2.22, Y_2 = 1.77, Y = 3.92). (**F**) Mean log(P_O)-*V* relations in 70 μM Ca^{2+} for all mutants involving Y332 or its interaction partners.

coupling. Second, that mutation of Y332 or its interaction partners produces energetically equivalent changes *C* and *D* without altering L_V or L_{Ca} indicates that the perturbed coupling mechanisms are not independent, but rather the opposite, strictly nonadditive. An additive mechanism requires that the energetic change in L produced by V or Ca^{2+} sensor activation is independent of the status of the other sensor (i.e., $\Delta G_{CD} = \Delta G_D$, and $\Delta G_{DC} = \Delta G_C$ in Fig. 6C). Thus, if resting V and Ca^{2+} sensors act independently through the YFF pathway to suppress opening, then disrupting that mechanism should increase not only L_0 but also L_{Ca} and L_V, leaving only the fully activated state $L_{Ca,V}$ unchanged. Furthermore, the energetic change in L_0 should equal the sum of the energetic changes in *C* or *D*, which, as indicated by blue lines in Fig. 6 (A and B), is clearly inconsistent with the effect of mutating Y332 or its interaction partners. By contrast, a strictly nonadditive model, which assumes that once one sensor is activated there is no additional effect of activating the other (i.e., $\Delta G_{CD} = \Delta G_{DC} = 0$ in Fig. 6C), predicts that disrupting this mechanism should have no effect on L_{Ca}, L_V, or $L_{Ca,V}$ and requires that the energetic contribution of the mechanism to *C* and *D* be equal, as observed experimentally, to satisfy detailed balance for the thermodynamic cycle ($\Delta G_C + \Delta G_{CD} = \Delta G_D + \Delta G_{DC}$) when $\Delta G_{CD} = \Delta G_{DC} = 0$. The latter is not a requirement of nonadditive mechanisms in general. For example, in Fig. 6C, if $\Delta G_{CD} = \Delta G_D - X$, and $\Delta G_{DC} = \Delta G_C - X$, where *X* represents the interaction energy between V- and Ca^{2+}-dependent coupling, there is no requirement that the magnitudes of ΔG_C and ΔG_D be related to satisfy detailed balance.

A key prediction of the strictly nonadditive model is that the YFF pathway should make no contribution to steady-state activity once V sensors or Ca^{2+} sensors are fully activated, as either stimulus should suffice to eliminate suppression of activity by this pathway. Consistent with this prediction, log(P_O)-*V* relations for Y332A and WT are virtually indistinguishable in 70 μM Ca^{2+} (Fig. 6E). Log(P_O)-*V* relations in 70 μM Ca^{2+} are essentially superimposable for all mutations involving Y332 or its interaction partners, although some are shifted to slightly more positive voltages than Y332 or WT (Fig. 6F).

The general idea that responses of BK channels to V and Ca^{2+} sensor activation are not strictly additive is not surprising, as V and Ca^{2+} sensors interact functionally and structurally (*7*, *12*) and various degrees of cooperativity have been reported between sensors in different subunits (*38*, *39*). However, the difference between these previously described interactions and the YFF pathway mechanism is as extreme as the difference between analog and digital electronic circuits. Rather than one sensor merely modulating the activity of another sensor, the results suggest that, within the YFF pathway, activation of one sensor can essentially decouple the other from the gate. Furthermore, the strictly nonadditive nature of the mechanism requires that its effect on activity be the same whether V or Ca^{2+} sensors are activated. Thus, this mechanism should contribute an "all-or-none" signal integration component analogous to the

function of a digital OR logic gate, which compares two inputs (e.g., V and Ca^{2+} sensor activation) and produces the same maximal output (increase in activity) when either one or both inputs are activated (a logic function).

YFF pathway is likely to couple sensor activation to opening through the RKK ring

The logic gate–like function of the YFF pathway represents a previously unknown and potentially unique mode of signal integration that places strong constraints on possible molecular mechanisms. That activation of one sensor (V or Ca^{2+}) prevents contribution of the other suggests that activation of the first sensor disrupts interactions such that either (i) the second sensor becomes decoupled from the YFF pathway or (ii) the YFF pathway becomes decoupled from the gate. In the first case, for example, it is conceivable that Ca^{2+} sensor activation could decouple V sensors from the αB-βC loop because the VSD/αB interface is altered by gating ring expansion. However, such a mechanism appears unlikely, as VSD/αB contact is increased rather than decreased upon Ca^{2+} binding (*17*) and there is no obvious structural basis for satisfying the inverse requirement that V sensor activation decouples Ca^{2+}-dependent gating ring expansion from the αB-βC loop. In the second case, one obvious candidate for decoupling the YFF pathway from the gate upon sensor activation would be disruption of the critical interaction between Y332 and the αB-βC loop upon movement of the latter. However, the constant structural relationship between Y332, F391, and F400 in the presence and absence of Ca^{2+} (Fig. 5C) indicates that this interaction is not dynamic but more like a link in chain that must be maintained to transduce sensor activation into C-linker movement and channel opening. On the other hand, decoupling the YFF pathway from the gate could be mediated by the RKK ring. This region, immediately adjacent to Y332 in the C-linker, forms a salt-bridge interaction through R329 with E321 in the S6 segment of an adjacent subunit in the closed hSlo1 structure but not in the Ca^{2+}-bound structure largely due to the movement of the αB-βC loop and C-linker (Fig. 7A). Thus, the RKK/S6 interaction represents a likely candidate to stabilize the CR state that can be disrupted by sensor activation and C-linker movement through the YFF pathway. Consistent with this hypothesis, mutation of R329 or K330 reduced *C* and *D* to a similar extent (Fig. 6D and Table 1). Although R329A and K330A do not follow the inverse fourth power relationship between L_0 and *C* or *D* (Fig. 6, A and B) observed for other YFF pathway mutations, this is understandable as RKK ring residues are proposed to interact with lipids in the open conformation such that hydrophobic substitutions increase P_0 more than polar substitutions (*34*). That is, Ala substitutions may increase L_0 by introducing interactions in the open conformation in addition to disrupting coupling. Therefore, we conclude that the effects of mutagenesis are consistent with a role for the RKK ring in the YFF pathway.

While the large >12-Å lateral movement of the αB-βC loop associated with Ca^{2+} binding in hSlo1 is clearly sufficient to disrupt interactions between the RKK ring and S6 and supports the proposed role of Ca^{2+} sensor activation in the YFF pathway, there is no direct structural evidence to indicate whether V sensor activation alone can perturb the RKK ring as no structures of Slo1 in the apo, V sensor–activated state exist. However, superposition of the Ca^{2+}-free and Ca^{2+}-bound structures suggests that the above noted rotation of the gating lever that is putatively driven by V sensor activation cannot occur without creating steric clash between S4-S5 linker and αB-βC loop if the gating ring remains in the Ca^{2+}-free conformation (fig. S6A), supporting the hypothesis that V sensor activation can move the αB-βC loop and thereby disrupt RKK ring interactions.

An allosteric model for multiple components of V- and Ca^{2+}-dependent coupling

The results indicate that components of Ca^{2+}- and V-dependent coupling mediated by the YFF pathway do not act independently, as assumed in the HA model. However, many features of WT Slo1 function appear consistent with the notion that Ca^{2+} and V exert independent or energetically additive effects on channel activity (*12*, *21*, *22*). To test whether the proposed YFF mechanism is consistent with these observations, we modified the HA model to include a nonadditive component of Ca^{2+}- and V-dependent coupling (Y) in addition to additive components (C and D; Fig. 7, B and C, Scheme 1). Scheme 1 describes the steady-state activity of Slo1 by the following equation, which is equivalent to the HA model when $Y = 1$.

$$P_O = \frac{L[1 + JD + KC + KJCDE/Y]^4}{L[1 + JD + KC + KJCDE/Y]^4 + [1 + J + K + KJE]^4} \quad (1)$$

$$\text{where } L = L_0 \exp\left(\frac{z_L V}{kT}\right); J = J_0 \exp\left(\frac{z_J V}{kT}\right); K = \frac{[Ca^{2+}]}{K_d}$$

K_d is the elementary Ca^{2+} dissociation constant when the channel is closed and V sensors are not activated, and z_L and z_J are partial charges associated with channel opening and V sensor activation, respectively.

The relationship among allosteric factors and equilibrium constants in Scheme 1 is illustrated in Fig. 7C by a diagram representing the four open and four closed states that can be accessed from rest by activating a single V and/or Ca^{2+} sensor within a functional unit, which includes an interacting pair of VSD and CTD from adjacent subunits. The channel is assumed to consist of four functional units that act independently. That interaction of V and Ca^{2+} sensors is confined to adjacent subunits is a simplifying assumption, consistent with the structural basis of the YFF mechanism. However, as noted below, disrupting the YFF pathway does not abolish interaction between V and Ca^{2+} sensors; therefore, multiple sensor/sensor interaction mechanisms may exist including between functional units, as suggested by recent gating current data (*40*). Parameters in Fig. 7C, other than Y, are arranged as in the HA model (*12*). One effect of the YFF mechanism is to decrease electromechanical coupling Y-fold when Ca^{2+} is bound (compare OR-OA and OR_{Ca}-OA_{Ca} transitions). To maintain detailed balance, this also requires that Ca^{2+}-dependent coupling is reduced Y-fold upon V sensor activation and the contribution of coupling to opening is reduced Y-fold when both sensors are activated (see OA-OA_{Ca} and CA_{Ca}-OA_{Ca} transitions), consistent with the nonadditive nature of the mechanism.

To determine parameters for Scheme 1 and gain more insight into the YFF mechanism, $\log(P_O)$-V relations for WT and Y332A were fit (Fig. 6E) with the assumption that Y332A abolishes the YFF contribution (i.e., $Y = 1$) such that Y332A can effectively be described by the HA model. Because Scheme 1 is defined in

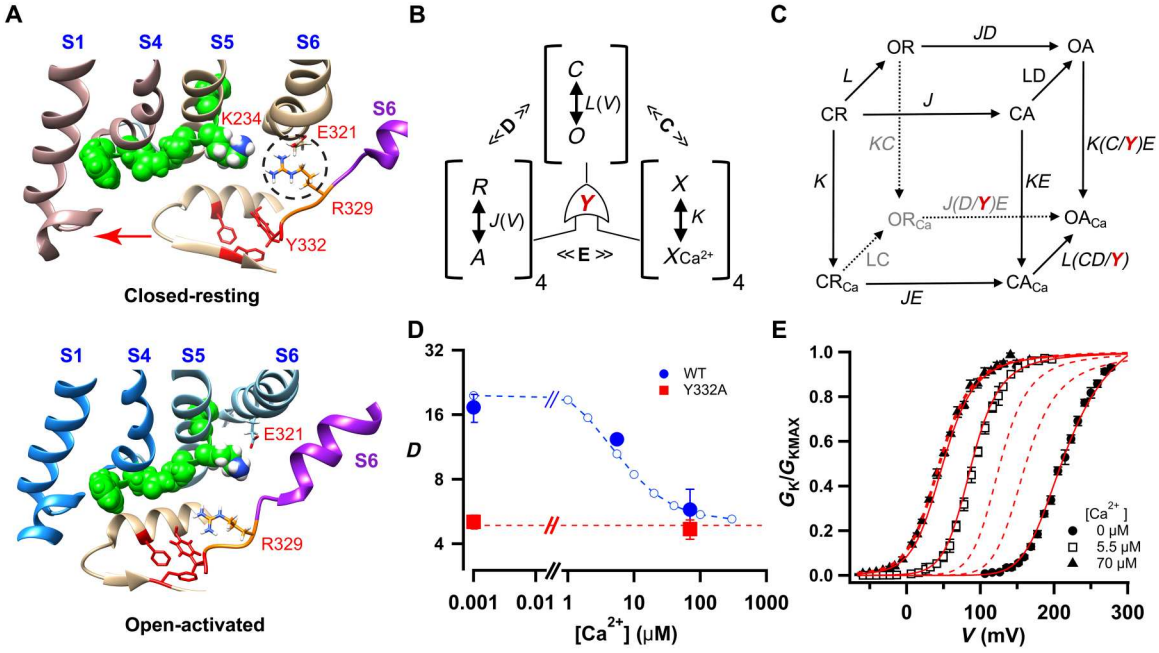

Fig. 7. A molecular logic gate mechanism mediated by the YFF pathway. (**A**) Structures of the αB-βC loop and C-linker from one subunit and VSD from the adjacent interacting subunit, with gating lever residues shown as space filling (green). In the apo closed conformation (top), interaction between R329 in the RKK ring (orange) and E321 in S6 suppresses opening. This interaction is broken when the αB-βC loop undergoes a lateral movement (arrow) upon gating ring expansion in the Ca^{2+}-bound conformation (bottom). (**B**) Scheme 1 is HA model modified to include a nonadditive component of V- and Ca^{2+}-dependent coupling *Y*, representing the YFF pathway mechanism. (**C**) The relationship among allosteric factors and equilibrium constants defined by Scheme 1 is illustrated by a diagram representing the four open and four closed states that can be accessed from rest by activating a single V and/or Ca^{2+} sensor within a functional unit. (**D**) Scheme 1 predicts Ca^{2+}-dependent decrease in electromechanical coupling for WT, but not Y332A, consistent with data. (**E**) Mean G_K-*V* relations for WT in 0, 5.5, and 70 μM Ca^{2+} are compared to predictions of Scheme 1 (solid curves) at these and additional concentrations (dashed curves: 0.5, 1.5, and 300 μM), showing that the model predicts little change in *G-V* shape with Ca^{2+} despite the decrease in electromechanical coupling. Curves were normalized to G_{KMAX} estimated by fitting each curve with a Boltzmann function, as is often done experimentally. Parameters for Scheme 1 (see fig. S7 legend) were equivalent to those determined in Fig. 6E.

terms of composite parameters such as *L*, *C*, and *D*, which include contributions from both the YFF pathway and other mechanisms, an alternative form of Scheme 1 was used (fig. S6B, Scheme 1b) to isolate the YFF contribution by rearranging parameters in terms of the HA model parameters for Y332A (L', K', J', C', D', and E') and *Y*. For example, setting $C' = C/Y$, $D' = D/Y$, and $L' = LY^4$ reflects the hypothesis that the YFF pathway increases both V- and Ca^{2+}-dependent coupling *Y*-fold by suppressing basal activity Y^4-fold (which is relieved upon V or Ca^{2+} sensor activation). That P_O of WT and Y332A at negative voltages in 0 Ca should differ by a factor of Y^4 directly constrains the value of $Y = 3.92$ used in Fig. 6E. However, two free parameters are required to fully describe the difference between WT and mutant as the YFF mechanism could potentially act to suppress basal activity by stabilizing the CR conformation or destabilizing the OR conformation. A consequence of these alternatives together with the reciprocal nature of sensor/gate interaction in allosteric models is that sensor activation must be suppressed in closed states and/or enhanced in open states, as represented by factors Y_1 and Y_2, respectively, in fig. S6B, where $Y = Y_1Y_2$, and Po can be expressed as

$$P_O = \frac{L'/Y^4[1 + Y_2(K'C' + J'D' + K'J'C'D'E')]^4}{L'/Y^4[1 + Y_2(K'C' + J'D' + K'J'C'D'E')]^4 + [1 + Y^{-1}(K' + J' + K'J'E')]^4} \quad (2)$$

If the YFF mechanism proposed in Scheme 1b and Eq. 2 is correct, then it should be possible to fit both WT and Y332A $\log(P_O)$-*V* relations with the same parameters, other than Y_1,Y_2. This is indeed the case and supports that Y332A primarily abolishes nonadditive coupling. In Fig. 6E, Y332A (0 and 70 μM Ca^{2+}) and WT (0, 5.5, and 70 μM Ca^{2+}) were fit, with L', K', J', C', D', and E' constrained to be identical for both channels (with $z_J = 0.58$, $z_{L'} = 0.28$), and Y_1 and Y_2 were allowed to vary for the WT with $Y_1 = Y_2 = 1$ for Y332A. Fitting the WT required that both Y_1 and Y_2 be greater than 1 because the 0 Ca^{2+} $\log(P_O)$-*V* relation for WT is shifted to more positive voltages than Y332A, consistent with an inhibition of V sensor activation in the closed conformation ($Y_1 > 1$), whereas the slope of $\log(P_O)$ (i.e., $q_a = kTd\ln(P_O)/dv$) achieves a limiting value at more negative voltages for WT than Y332A in 0 Ca^{2+} (fig. S6C, arrow), consistent with enhancement of voltage sensor activation in the open conformation ($Y_2 > 1$). The limiting V dependence of q_a provides a model-independent indication of the charge distribution for open channels (Q_O) (*12*), which is approximated by dashed Boltzmann function fits in fig. S6C. This relationship for Y332A is shifted by −62 mV in 70 μM Ca^{2+}, consistent with interaction between V and Ca^{2+} sensors represented by the allosteric factor E'. The WT exhibits a smaller shift of −37 mV, similar to a −43-mV shift previously reported for mSlo1 from an independent dataset (*12*), an effect that is accounted for by Scheme 1b when $Y_2 > 1$.

Scheme 1b not only accounts for the difference between WT and Y332A but also better fits the WT data in high Ca^{2+}, where the HA model tends to overestimate the steepness of the curves at $P_O > 0.1$ (Fig. 1, C and E) (*12*). This is because Scheme 1 and Ib predict a Ca^{2+}-dependent decrease in electromechanical coupling, consistent with the WT data (Fig. 7D), whereas the HA model assumes that *D* is constant. However, this model also reproduces several observations that have been taken as evidence that Ca^{2+} and V act independently including that the fractional increase in P_o is nearly V independent (e.g., Fig. 6E, WT 0 versus 5.5 μM Ca^{2+}) and normalized *G-V* relations maintain a similar shape in different Ca^{2+} (Fig. 7E). The reasons for this apparently simple behavior are in some regard paradoxically complex, as discussed below. However, one reason is that the YFF mechanism in Scheme 1 does not add any interaction between sensors at rest nor between sensors in different functional units; thus, deviations from the HA model are only evident under conditions where both sensors are highly activated.

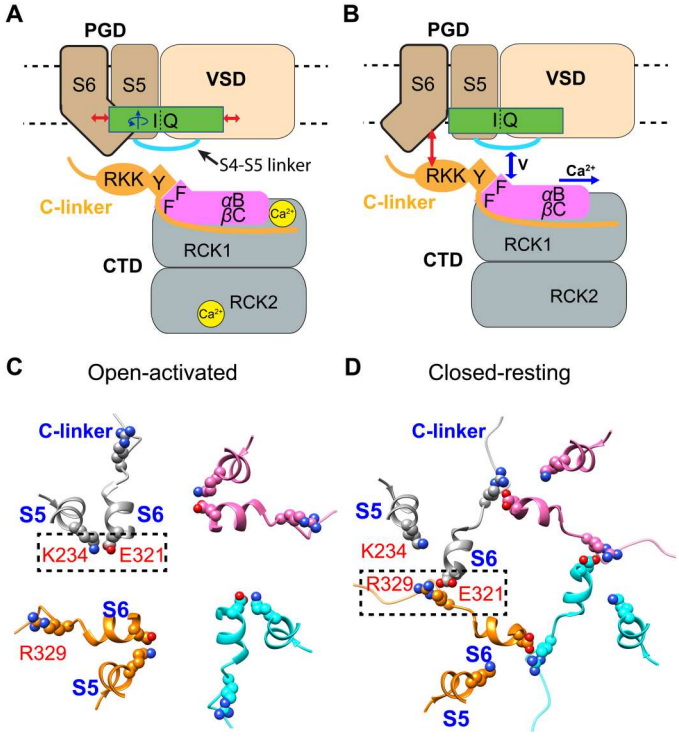

Fig. 8. Relationship between two electromechanical coupling pathways in Slo1. (**A**) Gating lever (green), immediately above the S4-S5 linker (cyan), includes S4 and S5 residues that are proposed to interact with the VSD and S6, respectively, in the same subunit (red arrows) in open-activated states to stabilize the open S6. Static interaction of Q222 and I233 at the S4/S5 interface helps maintain gating lever structure as it rotates about the S5 axis during V sensor activation. (**B**) The YFF pathway, composed of the αB-βC loop in RCK1 (pink) and proximal C-linker (orange), interacts with S6 in an adjacent subunit (red arrow) through the "RKK" ring when V and Ca^{2+} sensors are at rest to stabilize the closed conformation. However, movement of the αB-βC loop triggered by Ca^{2+} binding or V sensor activation (blue arrows) disrupts the stabilization of S6, owing to static interaction of Y332 with F391 and F400 at the C-linker/αB-βC loop interface. (**C** and **D**) Axial views of the cytoplasmic end of the hSlo1 pore in Ca^{2+}-bound open and apo closed conformations, respectively, with subunits in different colors, showing the contribution of E321 in S6 to different coupling pathways. (C) The gating lever stabilizes the open-activated conformation through intrasubunit salt-bridge interaction of E321 with K234 in S5. (D) The YFF pathway stabilizes the CR conformation through the intersubunit salt-bridge interaction of E321 with R329 in the RKK ring. These interactions depend not only on movement of S6 associated with opening but also on rotation of S5 or movement of the C-linker associated with V or Ca^{2+} sensor activation.

DISCUSSION

BK and K_V1 channels both exhibit strong electromechanical coupling between V sensor and pore domains (VSD and PGD) (*41*, *42*); however, the mechanisms, as highlighted by our results, are very different. The canonical mechanism for most K_V and structurally related Na_V and Ca_V channels, involving S6/S4-S5 linker interaction, represents a simple and efficient means to connect the most mobile parts of VSD and PGD and may also account for the apparent obligatory nature of coupling in these channels, as the S4-S5 linker is predicted or observed (*43*–*45*) to form a collar around the closed pore that could prevent opening at rest. However, such a mechanism is not well suited to BK channel function or structure. First, BK channels in some tissues must respond to Ca^{2+} when most V sensors are at rest; thus, any mechanism that prevents opening under these conditions would be counterproductive. Second, BK channels are less V dependent than K_V channels, and the VSD conformational change is smaller (*7*, *9*), precluding a K_V-like mechanism where S4 must undergo a large displacement perpendicular to the membrane in order for the S4-S5 linker to track the large conformational change in S6 (fig. S5A). Instead, we find that the intracellular ends of the VSD and S6 in Slo1 are coupled by two different pathways: a direct pathway within the TMD that stabilizes the open S6 conformation through S5 when V sensors are activated (fig. S8A), and an indirect pathway through the CTD that stabilizes the closed S6 at rest (fig. S8B). It may be that multiple pathways for electromechanical coupling are required in BK channels simply to produce strong coupling in the absence of direct steric interaction between VSD and S6, and our results do not rule out that additional pathways exist.

A gating lever to couple small VSD movement to opening

Vertical movement of the S4 segment during VSD activation in $K_V1.2$ channels is estimated to be as much as 16 Å (*43*, *44*), sufficient to drive the S4-S5 linker to directly affect S6 opening. However, the order-of-magnitude smaller vertical movement of S4 in Slo1 structures suggests that a different coupling mechanism is required. Our results reveal a mechanism that is consistent with the observed VSD conformational changes and nonswapped architecture of the Slo1 TMD. The bottom of S4 undergoes a tangential motion of ~6 Å that, together with strong S4/S5 interaction, results in a rotation of S5 that allows it to engage and stabilize the intracellular end of S6 in the open conformation (Fig. 8A). This mechanism is supported by reductions in electromechanical coupling by mutations of S4 (F223) and S6 (E321 and I322) and marked decreases in basal activity (L_0) by mutation of intervening residues in S5 (K235, L234, and I233) and S4 (Q222) that provide a continuous pathway between S4 and S6 in the open conformation. The intervening residues maintain a constant relationship with each other in Slo1 structures, apparently serving as a rigid gating lever to translate S4 movement into S5 rotation.

The gating lever mechanism is likely to account for the previously described effect on electromechanical coupling of a nearby S4

mutation E219R (*27*). However, whether perturbations in coupling produced by mutating more distal sites in the VSD (E180, D186, and R210) (*9*) or S6 (L312 and F315) (*46*–*48*) involve the same mechanism is unknown. Noncanonical mechanisms coupling the VSD to activation or inactivation in Shaker and other K_V channels have been reported involving S4/S5 interaction at various locations within the TMD (*49*–*51*). Related mechanisms could exist in Slo1, as S4 and S5 interact along their entire length, but, if so, are also likely to differ in detail from those in K_V channels owing to the smaller movement of S4 relative to S5 in Slo1. Likewise, noncanonical pathways appear to exist in other nonswapped channels with short S4-S5 linkers including EAG1 (K_V10.1), hERG1 (K_V11.1), and spHCN (*52*) and have been proposed to be mediated by S4/S5 or C-linker/VSD interactions (*53*, *54*), conceptually analogous to mechanisms we propose for Slo1, but differing greatly in detail.

An integrated component of V- and Ca^{2+}-dependent coupling through the CTD

The YFF pathway for electromechanical coupling, by contrast to the gating lever mechanism, relieves inhibition of basal activity upon VSD activation. Through this pathway, the S4-S5 linker, which rotates together with the gating lever, appears to interact indirectly with S6 through a series of noncovalent interactions involving the αB-βC loop of RCK1 and C-linker (Fig. 8B). This mechanism is supported by the ability of mutations in the RKK ring of the C-linker (R329A and K330A) to reduce electromechanical coupling and an apparently complete disruption of the pathway by mutation of interaction partners Y332 in the C-linker and F391, F400 in the αB-βC loop, as well as previously reported disruptions of electromechanical coupling by proline substitutions in αB (*17*). Although the YFF pathway does not prevent opening in the resting state, it strongly inhibits opening, reducing P_o by 236-fold or 3.28 kcal/mol (i.e., Y^4-fold from the Scheme 1b fit, Fig. 6E), most likely through the salt-bridge interaction of R329 with E321 in S6, evident in the apo closed structure (Fig. 7A). Mutation of K330, like R329, increases basal activity, suggesting that K330 may also stabilize the closed conformation and/or destabilize the open conformation.

In addition to its role in electromechanical coupling, the YFF pathway makes an energetically equivalent and nonadditive contribution to Ca^{2+}-dependent coupling. The nonadditive interaction between V- and Ca^{2+}-dependent coupling appears to result from a shared mechanism of action, involving suppression of channel activity through the RKK ring that is relieved by movement of the αB-βC loop in response to either Ca^{2+}-dependent gating ring expansion or V-dependent S4-S5 linker rotation. The shared nature of the pathway is supported by the observation that mutations in the above regions have energetically equivalent effects on V and Ca^{2+} coupling (Fig. 6D). Likewise, the ability of nearby mutations or deletions in the C-linker (G334A, Δ^{335}SYS^{337}) to disrupt both V- and Ca^{2+}-dependent coupling to a similar extent as Y332A suggests that they perturb the YFF pathway, presumably by disrupting the ability of Y332 to interact with the αB-βC loop. The G334A mutation is predicted to alter C-linker structure and potentially disrupt a hydrogen bond between the G334 backbone and R413 in RCK1 (fig. S5D). Although this interaction is not near the VSD/CTD interface, we speculate that it might be important for tethering the C-linker and Y332 close to the αB-βC loop, thereby stabilizing their interaction.

A major component of Ca^{2+}-dependent coupling is not mediated by C-linker tension

A prominent hypothesis, consistent with structural and functional studies (*7*, *24*), has been that Ca^{2+}-dependent coupling in Slo1 is mediated by the direct connection of CTD to S6 through the C-linker. That is, gating ring expansion driven by Ca^{2+} binding pulls on the C-linker, applying tension on S6, which favors the open conformation. However, our results indicate that Ca^{2+}-dependent coupling mediated by the YFF mechanism bypasses the covalent connection between CTD and PGD while accounting for a majority of Ca^{2+}-dependent coupling.

In the YFF pathway, Ca^{2+}-dependent gating ring expansion and the resulting lateral movement of the αB-βC loop is transmitted via interaction with Y332 to the C-linker of the same subunit. C-linker movement is then transmitted to the S6 segment of an adjacent subunit through disruption of interaction between the RKK ring and S6 (Fig. 8B). In theory, it seems reasonable that C-linker movement driven by the YFF pathway might also increase channel activity by pulling directly on S6 in the same subunit. However, if that is the case, the YFF pathway should contribute to P_O in saturating Ca^{2+}, when the αB-βC loop would presumably exert maximal tension on the C-linker, inconsistent with the observation that mutating any combination of Y332, F391, or F400 disrupts coupling without appreciably altering P_O at negative voltages in 70 μM Ca^{2+} (Fig. 6F).

Although the effects on V- and Ca^{2+}-dependent coupling of Y332A are energetically equivalent (3.28 kcal/mol, from Scheme 1b fits, Fig. 6E), the fractional decrease in coupling energy for Ca^{2+} (62%) is larger than for voltage (48%), reflecting that the total coupling energy is less for Ca^{2+} (ΔG_C = 5.3 kcal/mol) than for voltage (ΔG_D = 6.8 kcal/mol). Thus, the YFF pathway appears to represent the primary mechanism for Ca^{2+}-dependent coupling. However, the remaining component of Ca^{2+}-dependent coupling (*C′* in Scheme 1b) may still be mediated by the covalent CTD/PGD connection and changes in C-linker tension as previously proposed (*24*). While mutation of Y332 presumably decouples the C-linker from αB-βC loop, it does not decouple the C-linker from covalent and noncovalent interactions with other parts of the gating ring that move upon Ca^{2+} binding. Unlike Y332A, the C-linker deletion ΔSYS increases P_O in 70 μM Ca^{2+} by an order of magnitude (Fig. 1E), consistent with the idea that activity can be enhanced by increases in linker tension. Although our results suggest that effects on gating of deletions and insertions in the C-linker are more complicated than previously proposed and may include changes in allosteric coupling, the reported ability of insertions to decrease P_o cannot readily be explained in terms of a disruption of the YFF pathway, and is again consistent with the idea that linker tension contributes to channel activity. Additional work will be needed to resolve the different mechanisms for Ca^{2+}-dependent coupling, whether they interact with each other, and their relationship to the two Ca^{2+}-binding sites in each subunit.

The relationship between gating lever and YYF pathways

Although the two identified mechanisms for electromechanical coupling are structurally distinct, they share some common elements including a dependence on the movement of the gating lever and S4-S5 linker associated with VSD activation and interactions with E321 in S6. The latter, illustrated in Fig. 8 (C and D), helps summarize the relationship between these mechanisms.

Both pathways are likely to involve multiple interactions with S6 (e.g., Fig. 3C); however, E321 represents a common and potentially strong site of state-dependent salt-bridge interaction. The gating lever pathway through interaction of K234 with E321 helps stabilize the open conformation (Fig. 8, A and C). Conversely, when both V and Ca^{2+} sensors are in resting states, the YFF pathway stabilizes the closed conformation through interaction of R329 with E321 (Fig. 8, B and D). In both cases, the interactions that stabilize the closed or open conformations are dependent not only on the C-O transition of S6 but also on the position of the C-linker or rotational orientation of S5 that is linked to the activation state of the VSD.

The nature and role of V and Ca^{2+} sensor interaction in BK channel gating

The logic gate–like integration of V and Ca^{2+} signaling by the YFF pathway is a potentially unique mechanism that raises many interesting questions regarding its physiological role and evolution. While we cannot speculate about the latter, the most obvious role of the mechanism is to enhance both V- and Ca^{2+}-dependent coupling, and it may also act paradoxically to simplify the physiological response to V and Ca^{2+}, as discussed below.

The YFF mechanism has complex biophysical implications in that it represents an interaction between V and Ca^{2+} sensors that depends on channel opening. This can be understood by considering that the electromechanical coupling factor D reflects the ratio of the equilibrium constants for V sensor activation when the pore is open or closed [i.e., $D = J(O)/J(C)$] (*12*). Thus, a reduction in D upon Ca^{2+} binding (Fig. 7D) implies that $J_{Ca}(O)/J_{Ca}(C) < J(O)/J(C)$ or equivalently $J_{Ca}(O)/J(O) < J_{Ca}(C)/J(C)$. That is, the ability of Ca^{2+} to enhance V sensor activation should be greater in the closed state than in the open state, and a similar conclusion follows for the ability of V sensor activation to perturb Ca^{2+}-binding affinity. This distinguishes the YFF interaction mechanism from that represented by the E-factor in the HA model or E' in Scheme 1b, which is defined as an interaction between V and Ca^{2+} sensors that is independent of opening and has no effect on V- or Ca^{2+}-dependent coupling. The latter was assumed in the HA model in part because the value of D in high Ca^{2+} could not be well constrained with the 20-mV measurement intervals used by Horrigan and Aldrich (*12*). However, by using smaller 10-mV intervals and a model-independent estimate ($q_{\lambda MAX}$ method), we show here that D is decreased with Ca^{2+}, supporting that a component of V/Ca^{2+} sensor interaction is dependent on opening. This approach also indicates that D is not Ca^{2+} dependent once the YFF pathway is disrupted (Fig. 7D; Y332A), implying that the remaining interaction of V and Ca^{2+} sensors is independent of opening. Another reason why V/Ca^{2+} sensor interaction was assumed to be independent of opening in the HA model is that the Ca^{2+}-dependent shift in the charge distribution for closed channels (ΔV_{HC}), from mSlo1 gating current, was found to be comparable to the approximate −40-mV shift in ΔV_{HO} indicated by the q_a-V relation (e.g., fig. S6C) (*12*). However, this conclusion has recently been brought into question as a much larger ΔV_{HC} of −145 mV was reported for hSlo1 (*40*). Additional investigation of gating currents in WT and Y332A Slo1 will be required to evaluate the impact of the YFF pathway on ΔV_{HC} and determine whether the above disparate estimates, which bracket the prediction of Scheme 1 (ΔV_{HC} = −101 mV), can be accounted for by differences in the Slo1 orthologs and/or expression systems used.

Despite the added biophysical complexity of the YFF mechanism, Scheme 1 predicts a simpler response to V and Ca^{2+} than the HA model under physiological conditions (fig. S7). The log(P_O)-V relations at 0 to 300 μM Ca^{2+} are similar for both models but diverge at $P_O > 0.1$ in the presence of Ca^{2+} (fig. S7A). This difference is most obvious on a linear scale (fig. S7B), which shows that P_O-V, corresponding to macroscopic G-V relations, becomes steeper in Ca^{2+} for the HA model but less so for Scheme 1. A plot of the maximal GV slope (fig. S7C), normalized to 0 Ca^{2+}, shows that the Ca^{2+}-dependent increase in slope for Scheme 1 is less than half that of the HA model. The increase in slope occurs because both models predict that the maximal V dependence of channel activity (i.e., $q_{\lambda MAX}$) occurs at $V < V_{0.5}$ in 0 Ca^{2+} such that an increase in P_O by Ca^{2+} tends to raise steeper parts of curve into the macroscopic range. In Scheme 1, however, the YFF mechanism acts to partially counteract this effect through Ca^{2+}-dependent suppression of electromechanical coupling. Likewise, the increase in the C-O equilibrium by Ca^{2+} is less V dependent for Scheme 1 in the physiological voltage range than for the HA model (fig. S7D), owing to the ability of the YFF mechanism to suppress Ca^{2+}-dependent coupling upon V sensor activation. Thus, the net effect of the YFF mechanism is to make the V sensitivity of the channel less Ca^{2+} dependent and the Ca^{2+} sensitivity less V dependent. Whether or not this behavior is important physiologically, it helps explain why simpler mechanisms such as a V-dependent Monod-Wyman-Changeux model (*21*) can successfully describe many features of the macroscopic G-V data.

Implications for HA model analysis

The HA model (Fig. 1F) and methods to determine its parameters (*12*) have been used extensively to define mechanisms of BK channel modulation by mutations, auxiliary subunits, and small molecules (*55*). Our results show that the allosteric interactions in the HA model each represent multiple pathways that can be described by Scheme 1 (Fig. 7B). Variants of the HA model have also been proposed to account additional complexity, such as the presence of two high-affinity Ca^{2+}-binding sites per subunit (*56*). Detailed schemes are required to account for the effects of mutations that disrupt individual coupling pathways or binding sites and to test hypotheses about the mechanisms involved, as we have done here. However, in the absence of these mutant data, constraining additional free parameters can be difficult, and the simplest model may be preferred (*57*). Therefore, we expect that the HA model will continue to be used for the purpose of distinguishing between changes in the function of sensor or gate domains, or changes in their interaction, with the understanding that the function or interaction that is altered could be mediated by multiple mechanisms.

The main limitation of HA model analysis revealed by our results is that it may underestimate the interaction between V and Ca^{2+} sensors. This is because the two mechanisms proposed to mediate this interaction in Scheme 1 can produce opposing Ca^{2+}-dependent shifts in the log(P_o)-V relation. Thus, HA model analysis may detect changes in sensor/sensor coupling, but quantifying those changes would require additional analysis in terms of Scheme 1. On the other hand, estimates of total sensor/gate coupling (C and D) based on the HA model or Scheme 1 are identical, because Scheme 1 reduces to the HA model under the conditions used to measure C or D (i.e., at extreme negative voltages or in 0 Ca^{2+}).

This is evident from Eq. 1, as the terms including the allosteric factor Y are eliminated if either J or K is set to zero, which corresponds to having V or Ca^{2+} sensors at rest, respectively.

Allosteric coupling and the role of CPDs

The suggestion that multiple pathways for V- or Ca^{2+}-dependent coupling may exist in Slo1 has been made previously (*7*, *8*, *17*). Our study extends this previous work by identifying key pathways and defining the underlying molecular mechanisms. We provide insight not only into BK channel function but also into the nature of sensor/gate interaction and how to define such pathways. In general, energetic coupling between sensor and gate requires that interactions that are dependent on the conformation of both domains occur (*37*). Thus, coupling can potentially be mediated by state-dependent interactions at interfaces between moving parts of sensor and PGD, as proposed for the canonical electromechanical mechanism, or by covalent linkers that connect such domains, as previously proposed for the Ca^{2+}-dependent activation of Slo1 (*24*). However, our results reveal a more complex distributed process whereby CPDs, assembled by noncovalent interactions, act as adapters to link the most mobile parts of sensor and gate, with state-dependent interactions occurring at sensor/CPD and CPD/S6 interfaces (Fig. 8, A and B). That allosteric coupling can involve a complex series of interactions or indirect pathways is not surprising. It has been argued that allosteric interactions in many regulatory proteins may be mediated by the folding and unfolding of intrinsically disordered domains rather than well-defined pathways and interactions (*58*). However, Slo1 appears to represent a counterexample to this hypothesis as CPDs are well defined structurally and appear to transmit sensor movement to the pore through rigid-body motions.

The involvement of CPDs also complicates the delineation of coupling pathways. While it is often assumed that allosteric coupling occurs at domain-domain interfaces and, conversely, that effects on gating of mutating these interfaces are due to changes in coupling, these are oversimplifying assumptions, at least in the case of Slo1. Ala scans of the S4-S5 linker region revealed many sites in Slo1 at VSD/PGD or VSD/CTD interfaces that perturb gating without altering electromechanical coupling, including mutations in the PGD (V236A) or CTD (E386A/E388A) that perturb V sensor activation (J) and a VSD mutation (L224A) that alters the closed-open equilibrium (L_0). Thus, it cannot be assumed that a change in function due to mutation of a sensor/PGD interface reflects a change in coupling even if the mutation alters the function of an adjacent domain. Conversely, mutations that alter coupling do not always represent sites of state-dependent sensor/gate interaction. In particular, mutation of Y332 or its interaction partners (F391 and F400) in the CTD disrupts both V- and Ca^{2+}-dependent coupling, yet these residues maintain a constant relationship in resting and activated structures (Fig. 5C), implying that they have an essential role in maintaining the structural integrity of the YFF pathway and in communicating conformational changes between sensor and gate, but that state-dependent interactions occur elsewhere (Fig. 8B). Likewise, residues at the VSD/PGD interface in S4 (Q222) and S5 (I233) that strongly influence voltage-dependent gating appear to be part of the gating lever that links VSD and PGD by rigid-body rotation (fig. S4B), rather than sites of state-dependent interaction. In the case of the gating lever mechanism, the proposed sites of state-dependent interaction are not at the VSD/PGD interface, but rather within the VSD (F223/S1) and within the PGD (S6/S5), with the gating lever providing communication such that the interactions within each domain are dependent on both VSD activation and PGD opening (Fig. 8A). In conclusion, our results suggest that coupling mechanisms can be indirect and distributed and that resolving these mechanisms requires structure-function analysis that can distinguish changes in coupling from changes in sensor or gate equilibria, as well as structural information in different states to distinguish static and dynamic interactions.

MATERIALS AND METHODS

Experimental design

Allosteric coupling in mutant and WT Slo1 BK channels was evaluated by measuring steady-state activity over a wide range of voltage, $[Ca^{2+}]$, and P_O and fitting the results with the HA allosteric model (*12*) as well as using the $q_{\lambda MAX}$ method (see Supplementary Text) to provide an independent estimate of electromechanical coupling (D). P_O was determined from macroscopic and unitary currents measured with the patch clamp technique from excised macropatches containing hundreds of channels.

Channel expression and molecular biology

The mbr5 clone (*59*) of the mouse homolog of the Slo1 gene (mSlo1) was expressed in *Xenopus* oocytes. Oocytes were injected with ~0.5 to 50 ng of complementary RNA (cRNA), incubated at 18°C, and studied 2 to 7 days after injection. The use of *Xenopus laevis* was approved by the Institutional Animal Care and Use Committee of Baylor College of Medicine. Site-directed mutagenesis was performed with the QuikChange method (Stratagene) and confirmed by sequencing.

Electrophysiology and data analysis

Patch clamp experiments were performed in the inside-out configuration at room temperature (21° to 24°C) using an Axopatch 200B amplifier (Axon Instruments), PATCHMASTER acquisition software (HEKA), and Igor Pro software (WaveMetrics Inc., Lake Oswego, OR) for graphing and data analysis. Patch pipettes were pulled from PG10150-4 glass (World Precision Instruments) and coated with wax (KERR Sticky Wax). The external pipette solution contained 140 mM K-methanesulfonic acid (K-MES), 2 mM $MgCl_2$, 6 mM HCl, and 20 mM 4-(2-hydroxyethyl)-1-piperazineethanesulfonic acid (HEPES). The internal solution contained 140 mM K-MES and 20 mM HEPES. In addition, "0 Ca^{2+}" solution contained 5 mM ethyleneglycol-O, O'-bis(2-aminoethyl)-N, N, N', N'-tetraacetic acid , reducing free Ca^{2+} to an estimated 0.8 nM. Solutions containing Ca^{2+} were buffered with 5 mM N-(2-Hydroxyethyl)ethylenediamine-N, N′,N2-triacetic acid, and free $[Ca^{2+}]$ was measured with a Ca^{2+} electrode (Orion Research Inc.). Ca^{2+} was added as $CaCl_2$, and $[Cl^-]$ was adjusted to 10 mM with HCl. (+)-18-Crown-6-tetracarboxylic acid (40 μM) was added to chelate contaminant Ba^{2+}. The pH of all solutions was adjusted to 7.2 with MES.

Currents were filtered at 20 kHz with an eight-pole Bessel filter (Frequency Device Inc.) and sampled at 200 kHz with an ITC-18 A/D converter (Instrutech). Macroscopic currents were evoked by 20- to 30-ms pulses at 10-mV intervals from a holding potential of −80 mV and leak-subtracted by a P/4 protocol (*60*). Conductance was determined from tail currents at −80 mV and normalized by

G_{KMAX} measured in 70 μM Ca^{2+} to estimate P_O. Consistent with the assumption that G_{KMAX} reflects maximal activation (i.e., P_{OMAX}), G_K for all mutants saturated with voltage in 70 μM Ca^{2+}. According to the HA model, saturation can only occur when $P_O = P_{OMAX}$, because the C-O equilibrium constant L is intrinsically V dependent. Thus, even when V sensors are fully activated, if $P_O < P_{OMAX}$, G_K should increase according to the weak V dependence of L (z_L), as observed previously for some VSD mutants in 0 Ca^{2+} (*9*). P_{OMAX} measured by single-channel recording for several key mutants was confirmed to be >0.8, like WT (fig. S2C). The electrode's resistance in the bath solution (1.5 to 2.5 megohms) was used as an estimate of series of resistance (R_S) for correcting the voltage at which macroscopic I_K was recorded. Activity at low P_O in macropatches was determined from steady-state recordings of 5-s duration at V < +80 mV, or 0.5 s at higher V, that were digitally filtered at 5 kHz. NP_O was determined from all-points amplitude histograms by measuring the fraction of time spent (P_K) at each open level (K) using a half-amplitude criterion and summing their contributions, and N was estimated from G_{KMAX}.

Mean log(P_O)-V relations were determined by averaging log(P_O)-V relations from at least three patches per condition, after shifting individual curves to the mean $V_{0.5}$ for that condition, as described previously (*9*). Data were averaged in 10-mV bins and plotted against mean voltage. Parameters for the HA model or other schemes were determined by simultaneously fitting mean log(P_O)-V and q_a-V relations based on least squares criteria, weighted by variance. Mean activation charge displacement [$q_a = kTd\ln(P_O)/dV$] was measured from the slope of the log(P_O)-V relation by linear regression over 30-mV intervals (~4 data points) and plotted against mean voltage.

Structural analysis

Apo (6V3G) and Ca^{2+}/Mg^{2+}-bound (6V38) hSlo1 structures (*8*) were displayed, analyzed, and aligned using UCSF Chimera with default criteria for identifying contacts, clashes, hydrogen bonding, and buried solvent-accessible surface.

Statistical analysis

Channel activity [P_O, log(P_O)] and measurements of $V_{0.5}$ or limiting slope (z_L) derived thereof are plotted as the mean ± SEM of individual patches ($N \geq 3$). Model parameters or measurements (e.g., q_a and q_λ) based on mean log(P_O)-V relations are plotted as mean ± SD determined from fits or from multiple estimation methods as described in the text for allosteric factors C and D. Statistical significance of changes in allosteric factors was not evaluated, as their error distribution is unknown. However, plots of electromechanical coupling (D) include lines 3 SDs from the WT mean as an indicator of large changes that are highly unlikely to be accounted for by variance in the measurement.

Supplementary Materials

This PDF file includes:

Supplementary Text
Figs. S1 to S8
Table S1

View/request a protocol for this paper from *Bio-protocol*.

REFERENCES AND NOTES

1. P. R. Adams, A. Constanti, D. A. Brown, R. B. Clark, Intracellular Ca^{2+} activates a fast voltage-sensitive K^+ current in vertebrate sympathetic neurones. *Nature* **296**, 746–749 (1982).
2. B. Lancaster, R. A. Nicoll, Properties of two calcium-activated hyperpolarizations in rat hippocampal neurones. *J. Physiol.* **389**, 187–203 (1987).
3. R. Robitaille, M. P. Charlton, Presynaptic calcium signals and transmitter release are modulated by calcium-activated potassium channels. *J. Neurosci.* **12**, 297–305 (1992).
4. R. Robitaille, M. L. Garcia, G. J. Kaczorowski, M. P. Charlton, Functional colocalization of calcium and calcium-gated potassium channels in control of transmitter release. *Neuron* **11**, 645–655 (1993).
5. J. E. Brayden, M. T. Nelson, Regulation of arterial tone by activation of calcium-dependent potassium channels. *Science* **256**, 532–535 (1992).
6. G. J. Perez, A. D. Bonev, J. B. Patlak, M. T. Nelson, Functional coupling of ryanodine receptors to KCa channels in smooth muscle cells from rat cerebral arteries. *J. Gen. Physiol.* **113**, 229–238 (1999).
7. R. K. Hite, X. Tao, R. MacKinnon, Structural basis for gating the high-conductance Ca^{2+}-activated K^+ channel. *Nature* **541**, 52–57 (2017).
8. X. Tao, R. MacKinnon, Molecular structures of the human Slo1 K^+ channel in complex with β4. *eLife* **8**, e51409 (2019).
9. Z. Ma, X. J. Lou, F. T. Horrigan, Role of charged residues in the S1-S4 voltage sensor of BK channels. *J. Gen. Physiol.* **127**, 309–328 (2006).
10. W. N. Zagotta, T. Hoshi, R. W. Aldrich, Shaker potassium channel gating. III: Evaluation of kinetic models for activation. *J. Gen. Physiol.* **103**, 321–362 (1994).
11. F. T. Horrigan, R. W. Aldrich, Allosteric voltage gating of potassium channels II. Mslo channel gating charge movement in the absence of Ca^{2+}. *J. Gen. Physiol.* **114**, 305–336 (1999).
12. F. T. Horrigan, R. W. Aldrich, Coupling between voltage sensor activation, Ca2+ binding and channel opening in large conductance (BK) potassium channels. *J. Gen. Physiol.* **120**, 267–305 (2002).
13. Z. Lu, A. M. Klem, Y. Ramu, Coupling between voltage sensors and activation gate in voltage-gated K^+ channels. *J. Gen. Physiol.* **120**, 663–676 (2002).
14. S. B. Long, E. B. Campbell, R. Mackinnon, Voltage sensor of Kv1.2: Structural basis of electromechanical coupling. *Science* **309**, 903–908 (2005).
15. X. Tao, R. K. Hite, R. MacKinnon, Cryo-EM structure of the open high-conductance Ca^{2+}-activated K^+ channel. *Nature* **541**, 46–51 (2017).
16. Y. Zhou, H. Yang, J. Cui, C. J. Lingle, Threading the biophysics of mammalian Slo1 channels onto structures of an invertebrate Slo1 channel. *J. Gen. Physiol.* **149**, 985–1007 (2017).
17. Y. Geng, Z. Deng, G. Zhang, G. Budelli, A. Butler, P. Yuan, J. Cui, L. Salkoff, K. L. Magleby, Coupling of Ca^{2+} and voltage activation in BK channels through the αB helix/voltage sensor interface. *Proc. Natl. Acad. Sci. U.S.A.* **117**, 14512–14521 (2020).
18. G. Zhang, Y. Geng, Y. Jin, J. Shi, K. McFarland, K. L. Magleby, L. Salkoff, J. Cui, Deletion of cytosolic gating ring decreases gate and voltage sensor coupling in BK channels. *J. Gen. Physiol.* **149**, 373–387 (2017).
19. F. T. Horrigan, Z. Ma, Mg^{2+} enhances voltage sensor/gate coupling in BK channels. *J. Gen. Physiol.* **131**, 13–32 (2008).
20. H. Yang, J. Shi, G. Zhang, J. Yang, K. Delaloye, J. Cui, Activation of Slo1 BK channels by Mg^{2+} coordinated between the voltage sensor and RCK1 domains. *Nat. Struct. Mol. Biol.* **15**, 1152–1159 (2008).
21. D. H. Cox, J. Cui, R. W. Aldrich, Allosteric gating of a large conductance Ca-activated K^+ channel. *J. Gen. Physiol.* **110**, 257–281 (1997).
22. J. Cui, R. W. Aldrich, Allosteric linkage between voltage and Ca^{2+}-dependent activation of BK-type mslo1 K^+ channels. *Biochemistry* **39**, 15612–15619 (2000).
23. G. Budelli, Y. Geng, A. Butler, K. L. Magleby, L. Salkoff, Properties of Slo1 K^+ channels with and without the gating ring. *Proc. Natl. Acad. Sci. U.S.A.* **110**, 16657–16662 (2013).
24. X. Niu, X. Qian, K. L. Magleby, Linker-gating ring complex as passive spring and Ca^{2+}-dependent machine for a voltage- and Ca^{2+}-activated potassium channel. *Neuron* **42**, 745–756 (2004).
25. S. Chowdhury, B. Chanda, Deconstructing thermodynamic parameters of a coupled system from site-specific observables. *Proc. Natl. Acad. Sci. U.S.A.* **107**, 18856–18861 (2010).
26. D. Sigg, A linkage analysis toolkit for studying allosteric networks in ion channels. *J. Gen. Physiol.* **141**, 29–60 (2013).
27. G. Zhang, H. Yang, H. Liang, J. Yang, J. Shi, K. McFarland, Y. Chen, J. Cui, A charged residue in S4 regulates coupling among the activation gate, voltage, and Ca^{2+} sensors in BK channels. *J. Neurosci.* **34**, 12280–12288 (2014).
28. F. T. Horrigan, S. H. Heinemann, T. Hoshi, Heme regulates allosteric activation of the Slo1 BK channel. *J. Gen. Physiol.* **126**, 7–21 (2005).
29. Y. Liu, M. Holmgren, M. E. Jurman, G. Yellen, Gated access to the pore of a voltage-dependent K^+ channel. *Neuron* **19**, 175–184 (1997).

30. J. Thompson, T. Begenisich, Selectivity filter gating in large-conductance Ca^{2+}-activated K^+ channels. *J. Gen. Physiol.* **139**, 235–244 (2012).
31. C. M. Wilkens, R. W. Aldrich, State-independent block of BK channels by an intracellular quaternary ammonium. *J. Gen. Physiol.* **128**, 347–364 (2006).
32. Z. Jia, M. Yazdani, G. Zhang, J. Cui, J. Chen, Hydrophobic gating in BK channels. *Nat. Commun.* **9**, 3408 (2018).
33. E. C. Law, H. R. Wilman, S. Kelm, J. Shi, C. M. Deane, Examining the conservation of kinks in alpha helices. *PLOS ONE* **11**, e0157553 (2016).
34. Y. Tian, S. H. Heinemann, T. Hoshi, Large-conductance Ca^{2+}– and voltage-gated K^+ channels form and break interactions with membrane lipids during each gating cycle. *Proc. Natl. Acad. Sci. U.S.A.* **116**, 8591–8596 (2019).
35. C. A. Hunter, J. Singh, J. M. Thornton, π-π interactions: The geometry and energetics of phenylalanine-phenylalanine interactions in proteins. *J. Mol. Biol.* **218**, 837–846 (1991).
36. C. A. Hunter, J. K. M. Sanders, The nature of .pi.-.pi. interactions. *J. Am. Chem. Soc.* **112**, 5525–5534 (1990).
37. F. T. Horrigan, Perspectives on: Conformational coupling in ion channels: Conformational coupling in BK potassium channels. *J. Gen. Physiol.* **140**, 625–634 (2012).
38. X. Qian, X. Niu, K. L. Magleby, Intra- and intersubunit cooperativity in activation of BK channels by Ca^{2+}. *J. Gen. Physiol.* **128**, 389–404 (2006).
39. C. Shelley, X. Niu, Y. Geng, K. L. Magleby, Coupling and cooperativity in voltage activation of a limited-state BK channel gating in saturating Ca^{2+}. *J. Gen. Physiol.* **135**, 461–480 (2010).
40. Y. Lorenzo-Ceballos, W. Carrasquel-Ursulaez, K. Castillo, O. Alvarez, R. Latorre, Calcium-driven regulation of voltage-sensing domains in BK channels. *eLife* **8**, e44934 (2019).
41. F. T. Horrigan, J. Cui, R. W. Aldrich, Allosteric voltage gating of potassium channels I. Mslo ionic currents in the absence of Ca^{2+}. *J. Gen. Physiol.* **114**, 277–304 (1999).
42. L. D. Islas, F. J. Sigworth, Voltage sensitivity and gating charge in Shaker and Shab family potassium channels. *J. Gen. Physiol.* **114**, 723–742 (1999).
43. S. B. Long, X. Tao, E. B. Campbell, R. MacKinnon, Atomic structure of a voltage-dependent K^+ channel in a lipid membrane-like environment. *Nature* **450**, 376–382 (2007).
44. M. M. Pathak, V. Yarov-Yarovoy, G. Agarwal, B. Roux, P. Barth, S. Kohout, F. Tombola, E. Y. Isacoff, Closing in on the resting state of the shaker K^+ channel. *Neuron* **56**, 124–140 (2007).
45. G. Wisedchaisri, L. Tonggu, E. McCord, T. M. Gamal El-Din, L. Wang, N. Zheng, W. A. Catterall, Resting-state structure and gating mechanism of a voltage-gated sodium channel. *Cell* **178**, 993–1003.e12 (2019).
46. Y. Wu, Y. Xiong, S. Wang, H. Yi, H. Li, N. Pan, F. T. Horrigan, Y. Wu, J. Ding, Intersubunit coupling in the pore of BK channels. *J. Biol. Chem.* **284**, 23353–23363 (2009).
47. B. Wang, R. Brenner, An S6 mutation in BK channels reveals beta1 subunit effects on intrinsic and voltage-dependent gating. *J. Gen. Physiol.* **128**, 731–744 (2006).
48. W. Carrasquel-Ursulaez, G. F. Contreras, R. V. Sepulveda, D. Aguayo, F. Gonzalez-Nilo, C. Gonzalez, R. Latorre, Hydrophobic interaction between contiguous residues in the S6 transmembrane segment acts as a stimuli integration node in the BK channel. *J. Gen. Physiol.* **145**, 61–74 (2015).
49. C. A. Bassetto, J. L. Carvalho-de-Souza, F. Bezanilla, Molecular basis for functional connectivity between the voltage sensor and the selectivity filter gate in Shaker K^+ channels. *eLife* **10**, e63077 (2021).
50. A. I. Fernandez-Marino, T. J. Harpole, K. Oelstrom, L. Delemotte, B. Chanda, Gating interaction maps reveal a noncanonical electromechanical coupling mode in the Shaker K^+ channel. *Nat. Struct. Mol. Biol.* **25**, 320–326 (2018).
51. P. Hou, P. W. Kang, A. D. Kongmeneck, N. D. Yang, Y. Liu, J. Shi, X. Xu, K. M. White, M. A. Zaydman, M. A. Kasimova, G. Seebohm, L. Zhong, X. Zou, M. Tarek, J. Cui, Two-stage electro-mechanical coupling of a KV channel in voltage-dependent activation. *Nat. Commun.* **11**, 676 (2020).
52. J. Cowgill, B. Chanda, Mapping electromechanical coupling pathways in voltage-gated ion channels: Challenges and the way forward. *J. Mol. Biol.* **433**, 167104 (2021).
53. J. Cowgill, V. A. Klenchin, C. Alvarez-Baron, D. Tewari, A. Blair, B. Chanda, Bipolar switching by HCN voltage sensor underlies hyperpolarization activation. *Proc. Natl. Acad. Sci. U.S.A.* **116**, 670–678 (2019).
54. M. D. Clark, G. F. Contreras, R. Shen, E. Perozo, Electromechanical coupling in the hyperpolarization-activated K^+ channel KAT1. *Nature* **583**, 145–149 (2020).
55. T. Hoshi, S. H. Heinemann, Modulation of BK channels by small endogenous molecules and pharmaceutical channel openers. *Int. Rev. Neurobiol.* **128**, 193–237 (2016).
56. T. B. Sweet, D. H. Cox, Measurements of the BKCa channel's high-affinity Ca^{2+} binding constants: Effects of membrane voltage. *J. Gen. Physiol.* **132**, 491–505 (2008).
57. F. T. Horrigan, T. Hoshi, Models of ion channel gating, in *Handbook of Ion Channels*, J. Zheng, M. C. Trudeau, Eds. (CRC Press, 2015), pp. 83–101.
58. V. J. Hilser, J. O. Wrabl, H. N. Motlagh, Structural and energetic basis of allostery. *Annu. Rev. Biophys.* **41**, 585–609 (2012).
59. A. Butler, S. Tsunoda, D. P. McCobb, A. Wei, L. Salkoff, mSlo, a complex mouse gene encoding "maxi" calcium-activated potassium channels. *Science* **261**, 221–224 (1993).
60. C. M. Armstrong, F. Bezanilla, Charge movement associated with the opening and closing of the activation gates of the Na channels. *J. Gen. Physiol.* **63**, 533–552 (1974).

Acknowledgments: We thank R. Aldrich for comments on the manuscript and J. Cui for providing some of the mutants (F391A, F395A, F400A, and Y401A). **Funding:** This work was supported by NIH grants R01NS042901 (F.T.H.) and R01GM127332 (F.T.H.). **Author contributions:** Conceptualization: F.T.H. and L.S. Methodology: F.T.H. Software: F.T.H. Investigation: L.S. Formal analysis: L.S. and F.T.H. Visualization: L.S. and F.T.H. Writing—original draft: L.S. Writing—review and editing: F.T.H. **Competing interests:** The authors declare that they have no competing interests **Data and materials availability:** All data needed to evaluate the conclusions in the paper are present in the paper and/or the Supplementary Materials. mSlo1 constructs can be provided by Baylor College of Medicine pending scientific review and a completed material transfer agreement. Requests for constructs should be submitted to F.T.H. at horrigan@bcm.edu.

Submitted 18 April 2022
Accepted 8 November 2022
Published 14 December 2022
10.1126/sciadv.abq5772